1 **Tau aggregates are RNA-protein assemblies that mis-localize multiple nuclear speckle**

2 **components**

3

4

5 Evan Lester[1,2], Felicia K. Ooi[3], Nadine Bakkar[4], Jacob Ayers[3], Amanda L. Woerman[5], Joshua
6 Wheeler[1,2], Robert Bowser[4], George A. Carlson[3,6], Stanley B. Prusiner[3,6,7], Roy Parker[1,8,9]
7
8 1. Department of Biochemistry, University of Colorado Boulder, CO, USA
9 2. Medical Scientist Training Program, University of Colorado Anschutz Medical Campus,
10 Aurora, CO, USA
11 3. Institute for Neurodegenerative Diseases, Weill Institute for Neurosciences, University of
12 California, San Francisco, San Francisco, CA, USA
13 4. Department of Neurobiology, Barrow Neurological Institute, Phoenix, AZ, USA
14 5. Department of Biology and Institute for Applied Life Sciences, University of Massachusetts
15 Amherst, Amherst, MA, USA
16 6. Department of Neurology, Weill Institute for Neurosciences, University of California, San
17 Francisco, San Francisco, CA, USA
18 7. Department of Biochemistry and Biophysics, University of California, San Francisco, San
19 Francisco, CA, USA
20 8. Howard Hughes Medical Institute, University of Colorado, Boulder, CO, USA
21 9. Corresponding author
22

23   **Abstract**

24   Tau aggregates contribute to neurodegenerative diseases including frontotemporal

25   dementia and Alzheimer's disease (AD). Although RNA promotes tau aggregation *in vitro*,

26   whether tau aggregates in cells contain RNA is unknown. We demonstrate in cell culture and

27   mouse brains that both cytosolic and nuclear tau aggregates contain RNA, with enrichment for

28   snRNAs and snoRNAs. Nuclear tau aggregates colocalize with and alter the composition,

29   dynamics, and organization of nuclear speckles, which are membraneless organelles involved in

30   pre-mRNA splicing. Moreover, several nuclear speckle components, including SRRM2,

31   mislocalize to cytosolic tau aggregates in cells, mouse brains, and patient brains with AD,

32   frontotemporal dementia (FTD), and corticobasal degeneration (CBD). Consistent with these

33   alterations we observe the presence of tau aggregates is sufficient to alter pre-mRNA splicing.

34   This work identifies tau alteration of nuclear speckles as a feature of tau aggregation that may

35   contribute to the pathology of tau aggregates.

36

2

Introduction

Fibrillar aggregates of the microtubule associated protein tau (tau) are seen in numerous neurodegenerative diseases collectively referred to as tauopathies (Orr et al., 2017). Tauopathies have a variety of etiologies ranging from mutations in tau that promote its aggregation, such as in the inherited frontotemporal dementia with parkinsonism-17 (FTDP-17), to environmental triggers such as head trauma giving rise to chronic traumatic encephalopathy (CTE), to the incompletely understood link between beta-amyloid and tauopathy in Alzheimer's disease (AD) (Aoyagi et al., 2019; Goedert et al., 1988; Wischik et al., 1988).

Several lines of evidence suggest that the formation and propagation of tau oligomers or aggregates is a key driver of toxicity in tauopathies. First, mutations that promote tau aggregation are causative in FTDP-17 (Goedert and Spillantini, 2000). Second, the rate of cognitive decline in AD is closely related to the rate of tau aggregate formation (Hanseeuw et al., 2019). Third, tau aggregates and tauopathy can be transmitted by inoculation in cells and mice (Aoyagi et al., 2019; Kaufman et al., 2016; Sanders et al., 2014; Woerman et al., 2016). Induction of tau aggregates in cell models also can be toxic (Sanders et al., 2014). Fourth, reduction of tau is neuroprotective in mouse models of AD (DeVos et al., 2018). Understanding how tau oligomers or aggregates form and how they induce neurotoxicity may lead to the development of therapeutics for numerous neurodegenerative diseases.

Tau is present in the human central nervous system as six splice isoforms. These isoforms differ in the number of N terminal inserts—0N, 1N, or 2N—and the number of microtubule repeat binding domains (RD)—3R or 4R (Buée et al., 2000; Park et al., 2016). The N terminal inserts

3

60 have been shown to impact tau's localization, interactions with membranes, spacing between

61 microtubules, and signal transduction (Brandt et al., 1995; Chen et al., 1992; Lee et al., 1998; Liu

62 and Götz, 2013). The positively charged RD has been shown to form the core of the amyloid fibrils

63 present in the brains of patients with tauopathies and this is also where the majority of disease

64 causing mutations are found (Buée et al., 2000; Falcon et al., 2018, 2019; Fitzpatrick et al., 2017;

65 Goedert, 2005; Wegmann et al., 2013; Zhang et al., 2020).

66

67   Several observations suggest RNA may affect the formation of tau aggregates. First, tau

68 binds RNA (Dinkel et al., 2015; Schröder et al., 1984; Wang et al., 2006; Zhang et al., 2017).

69 Second, *in vitro* RNA promotes the conversion of soluble tau into insoluble aggregated tau,

70 possibly because the negatively charged phosphate backbone of RNA can neutralize the positively

71 charged RD of tau (Ambadipudi et al., 2017; Dinkel et al., 2015; Kampers et al., 1996). Third, tau

72 immunopurifies with a number of RNA binding proteins in both the aggregated and unaggregated

73 states (Bai et al., 2013; Broccolini et al., 2000; Gunawardana et al., 2015; Hales et al., 2014a,

74 2014b; Hsieh et al., 2019; Meier et al., 2016). Fourth, tau aggregates in AD and Pick's disease

75 have been found to stain positive for RNA using RNA dyes (Ginsberg et al., 1997, 1998). Finally,

76 analysis of the RNAs interacting with tau in an unaggregated state by iCLIP suggests that tau

77 preferentially interacts with tRNAs (Zhang et al., 2017). Thus, important questions are whether

78 pathological tau aggregates contain RNA, and if so, what is the nature of those RNAs and what

79 are the possible physiologic or pathologic consequences of their interaction?

80

81   Herein, we investigated the RNA composition of tau aggregates in both cell culture and

82 mouse model systems. Similar to earlier results, we found that tau aggregates form in the cytosol

83 and the nucleus (Bukar Maina et al., 2016; Gil et al., 2017; Rady et al., 1995; Sanders et al., 2014;

84 Ulrich et al., 2018). We found that both cytosolic and nuclear tau aggregates contain RNA and are

85 enriched for RNAs involved in RNA splicing and modification including snRNAs and snoRNAs,

86 as well as repetitive Alu RNAs. We also found that nuclear tau aggregates contain snRNAs and

87 are concentrated in, and alter the composition, organization and dynamics of, splicing speckles,

88 which are non-membranous assemblies of RNA and protein containing nascent RNA transcripts

89 and splicing machinery (Galganski et al., 2017). Surprisingly, we discovered that the serine

90 arginine repetitive matrix protein 2 (SRRM2), a protein component of splicing speckles,

91 mislocalizes from nuclear splicing speckles to cytosolic tau aggregates in cellular models of

92 tauopathy, tauopathy mouse models, and patients with AD, frontotemporal lobar degeneration

93 (FTLD), and corticobasal degeneration (CBD). These extensive interactions of tau with splicing

94 speckles and the splicing machinery correlate with splicing alterations seen in cells that form tau

95 aggregates. This is notably similar to how cytosolic sequestration of RNA binding proteins such

96 as TDP-43 and FUS in amyotrophic lateral sclerosis (ALS) can lead to alterations in nuclear RNA

97 processing promoting neurodegeneration (Lagier-Tourenne et al., 2012; Polymenidou et al., 2011).

98

99   **RESULTS**

100   **Cytosolic and nuclear tau aggregates contain RNA**

101   To determine whether tau aggregates contain RNA, we employed a previously developed

102   HEK293 tau biosensor cell line (Holmes et al., 2014; Sanders et al., 2014). The HEK293 biosensor

103   cells express the 4R repeat domain (RD) of tau with the P301S mutation tagged with either cyan-

104   fluorescent protein (CFP) or yellow fluorescent protein (YFP). Fluorescent tau aggregates can be

105   induced in these HEK293 cells via lipofection of preformed non-fluorescent tau aggregates

106   isolated from the brains of mice expressing 0N4R tau with the P301S mutation (P301S mice,

107   Tg2541) (Holmes et al., 2014; Sanders et al., 2014). As previously seen (Sanders et al., 2014), we

108   observed fluorescent tau aggregates in both the cytosol and the nucleus of the HEK293 cells

109   following transfection of clarified brain homogenate from mice expressing P301S human tau, but

110   not from mice expressing wild-type (WT) tau (WT mice, Tg21221), which do not develop

111   tauopathy (Fig. 1A-B). Nuclear tau aggregates are not an artifact of the truncated K18 tau

112   expressed in HEK293 cells since we also observed the formation of both nuclear and cytosolic tau

113   aggregates in a tau seeding model expressing full length P301S 0N4R tau-YFP in H4 neuroglioma

114   cells (Fig. S1A, Supp. video 3). Consistent with these fluorescent bodies being insoluble tau

115   aggregates, fluorescence recovery after photobleaching (FRAP) revealed that both nuclear and

116   cytosolic tau aggregates are immobile and do not recover after photobleaching (Fig. S1B, C).

117

118   Using fluorescence in-situ hybridization (FISH) for poly(A) RNA we observed that

119   cytosolic and nuclear tau aggregates showed 1.5- and 1.72-fold enrichment of poly(A)+ RNA

120   staining, respectively (Figure S1D). We also examined the presence of poly(A) RNA in tau

121   aggregates in the brains of 6 month old P301S mice, in which transmissible tau aggregates start to

122   form at 1.5 months (Holmes et al., 2014; Yoshiyama et al., 2007). Unlike in humans, where tau

123   pathology develops in the frontal cortex, tau pathology in P301S mice tau pathology develops

124   primarily in the hindbrain (Johnson et al., 2017). Nuclear tau and tau aggregates have been

125   previously observed in the brains of mice and humans, however their function and relevance to

126   disease is poorly understood (Bukar Maina et al., 2016; Gil et al., 2017; Jiang et al., 2019; Liu and

127   Götz, 2013; Montalbano et al., 2020; Rady et al., 1995; Ulrich et al., 2018). We observed nuclear

128   tau aggregates in the hindbrain stain strongly for poly(A) RNA (Fig. 1C, S1E, S7A). We also

129   observed a redistribution of poly(A) signal to overlap with the cytosolic tau aggregates in P301S

130   mouse brains (Fig. 1C, S1E, S7A). Thus, in both mouse and cellular models of tau pathologies,

131   tau forms cytosolic tangles and nuclear puncta that contain RNA.

132

133   **Tau aggregates in HEK293 cells and mouse brains are enriched for snRNAs and snoRNAs**

134   To determine the identity of the RNAs present in tau aggregates, we first purified tau

135   aggregates from HEK293 tau biosensor cells using differential centrifugation and fluorescent

136   activated particle sorting (FAPS) and then sequenced the associated RNA (Fig. S2A-C). SYTO17

137   staining of the lysates post-sorting confirmed that RNA remained associated with the tau

138   aggregates (Fig. S2A). By comparing the abundance of RNAs in total RNA and tau aggregates,

139   we observed that tau aggregates contain a diverse transcriptome (Fig. 2A) and were enriched for

140   small non-coding RNAs, particularly snoRNAs and minor snRNAs (Fig. 2B). Some mRNAs were

141   also enriched in tau aggregates, notably mRNAs coding for voltage gated calcium channel

142   complex, histone proteins, centrosomal proteins, and proteins involved in splicing regulation (Fig.

143   S2D-E).

144

145   Analysis of RNAs expressed from multicopy genes using RepEnrich (Criscione et al.,

146   2014) showed enrichment of RNAs from the multicopy snoRNAs (U3, U17, and U8) and the

147   multicopy snRNAs (U2 and U1) (Figure S2F-G). Consistent with this observation, U1 snRNA has

148   previously been observed to be enriched in AD tau aggregates by PCR (Hales et al., 2014a).

149   Additionally, this analysis showed some enrichment of tRNAs, as previously observed with non-

150   aggregated tau (Zhang et al., 2017). We also observed enrichment of RNAs from specific types of

151   transposable elements, namely the hAT-Tip100 family of DNA transposable elements and Alu

152   elements (Fig. S2F-G).

153

154   **Tau aggregates in P301L mouse brain are also enriched for snRNAs**

155   To investigate whether tau aggregates in mouse brains contain similar RNAs to tau

156   aggregates identified in HEK293 cells, we fractionated mouse brains with a 1% sarkosyl extraction

157   followed by tau immunoprecipitation (IP) using the tau-12 antibody to isolate tau aggregates as

158   previously described (Diner et al., 2017) (Fig. S2H). Western blot analysis showed that the

159   sarkosyl extraction enriched for insoluble tau in the P301L mice (rTg4510) but not in the WT mice

160   (rTg21221) (Fig. S2I). To identify RNAs specifically enriched in the aggregated tau fraction, we

161   compared the enrichment of RNAs in the insoluble tau-12 IP relative to total RNAs between the

162   WT and P301L mice (Fig. 2C).

163

164   Analysis of RNAs enriched in tau aggregates isolated from mouse brain relative to total

165   RNA revealed an enrichment of specific RNAs, including snRNAs and snoRNAs in the P301L

166   tau IP samples (Fig. 2C, D). This is similar to the RNA composition of tau aggregates isolated

167   from HEK293 cells (Fig S2K). For example, we observed that snoRD115, snoRD104, snoRD70,

168   U2 snRNA, and U6 snRNA, were enriched in the P301L insoluble tau fraction (Fig. 2C). In

169   contrast to the HEK293 tau aggregates, only particular snoRNAs were enriched. This could be due

170   to a variety of factors including differences in the isoforms of tau expressed in the two models (RD

171   of tau in the HEK293 cells versus full-length 0N4R tau in the rTg4510 mice), the mutation in tau

172   itself (P301S in the HEK293 biosensor cells and P301L in the rTg4510 mice), or differences in

173   the RNA expression profiles of HEK293 cells and mouse neurons. The sarkosyl-insoluble fraction

174   from both the P301L and WT mice revealed little to no enrichment of snRNAs or minor snRNAs

175   suggesting that RNAs enriched in the tau-12 IP are interacting with aggregated tau rather than just

176   enriched in the insoluble fraction (Fig. S2J). Similar to HEK293 cells, we observed some mRNAs

177   enriched in tau aggregates from mouse brain (Figure S2L). Interestingly, some of the most

178   enriched mRNAs are components of the centrosome (PCNT, Cep250, Cep164, Cep131) (Delaval

179   and Doxsey, 2010; Graser et al., 2007), which is in agreement with previous work that has observed

180   cytosolic tau aggregates concentrating at the centrosomes (Sanders et al., 2014; Santa-Maria et al.,

181   2012). mRNAs coding for centrosomal proteins, such as PCNT, have previously been described

182   to be present at the centrosome where they are locally translated and could become ensnared in tau

183   aggregates (Sepulveda et al., 2018). Taken together, our results demonstrate that isolated

184   pathological tau aggregates in mouse brains are enriched for similar types of RNAs as the tau

185   aggregates in HEK293 cells including snRNAs and snoRNAs.

186

187   **Enriched RNAs localize to tau aggregates by fluorescence in-situ hybridization**

188   We used FISH to examine if RNA enriched in tau aggregates identified by RNA

189   sequencing localized to cytosolic and/or nuclear tau aggregates. We performed FISH for two

190   enriched snRNAs (U2 and RNU6ATAC), two enriched snoRNAs (snoRA73B and snoRD3A),

191 two depleted mRNAs (CENPQ and NUCKS1), and for the enriched Alu family of multicopy

192 RNAs (Fig. 3, S3). Interestingly, we observed that enrichment of specific RNAs differed with

193 respect to the localization of tau aggregates. Specifically, snoRD3A had a 2.05-fold enrichment

194 into cytosolic tau aggregates relative to bulk cytosol, while nuclear tau aggregates had a 1.35-fold

195 enrichment of snoRD3A relative to bulk nucleoplasm (Fig. 3A). For U2 snRNA, cytosolic and

196 nuclear tau aggregates had roughly the same fold enrichment over their respective compartments

197 (1.48 and 1.42) yet the absolute intensity of U2 snRNA in nuclear tau aggregates was 1.87-fold

198 higher than that of the cytosolic tau aggregates (Fig. 3B). In cells without tau aggregates, U2

199 snRNA localizes into discrete nuclear foci called splicing speckles, which are non-membranous

200 RNA-protein assemblies containing factors involved in mRNA splicing (Kota et al., 2008; Wagner

201 et al., 2004; Zhang et al., 2016). Nuclear colocalization of the splicing speckle associated snRNAs

202 with tau implies that nuclear tau aggregation is occurring in splicing speckles (see below).

203 Consistent with this observation, we also see colocalization of the enriched RNU6ATAC snRNA

204 in nuclear tau aggregates (Fig. S3A).

205

206 We also performed FISH for an Alu consensus sequence present in the Alu RNAs enriched

207 from the sequencing data (Fig. S2F-G) and found that Alu signal enriched into both nuclear and

208 cytosolic tau aggregates (Fig. S3C). Alu enrichment was greater in cytosolic aggregates (1.56-fold;

209 $p<0.0001$) than in nuclear aggregates (1.23-fold; $p=0.02$). In the nuclear aggregates, Alu intensity

210 was greatest on the periphery of the aggregates. The depleted mRNA NUCKS1 did not show

211 significant intensity enrichment into either nuclear or cytosolic tau aggregates (Fig. 3C). Similarly,

212 no positive localization correlation could be found for the depleted mRNA CENPQ and tau (Fig.

213 S3D). Thus, tau aggregates contain, and are enriched for, a diverse set of specific RNAs.

214

Nuclear tau aggregates colocalize with splicing speckles in HEK293 cells

Due to the bias in both the HEK293 and mouse tau aggregate transcriptomes towards nuclear snRNAs and snoRNAs, we explored whether nuclear tau aggregates localized to the nucleolus, where snoRNAs are concentrated, or splicing speckles, which are enriched in snRNAs (Spector and Lamond, 2011).

Three lines of evidence suggest that nuclear tau aggregates colocalize with splicing speckles. First, the canonical splicing speckle antibody SC35 localized with nuclear tau aggregates by immunofluorescence (IF). In IF, the SC35 antibody recognizes the splicing speckle protein, SRRM2 (Ilik et al., 2020), and in agreement with this specificity, an SRRM2-halo fusion protein also localizes to nuclear tau aggregates (Fig. 4A, Fig. S4A). Similarly, other components of nuclear speckles co-localize with nuclear tau aggregates (see below). Second, nuclear tau aggregates are enriched for poly(A) RNA (Fig. 1C, S1D-E, Supp. Video 1, 2) and splicing speckle associated RNAs including U2 snRNA (Fig. 3B, S2F) (Huang et al., 1994). Third, consistent with tau accumulating in splicing speckles and not with other nuclear RNA foci, nuclear tau aggregates do not colocalize with the nucleolar markers fibrillarin and RPF1 (Kiss, 2002) (Fig. S4B-C). In the brains of P301S (Tg2541) mice, we also observe pTau(S422) signal colocalizing with both SRRM2 and poly(A) in the nucleus (Fig. S7A). Thus, nuclear tau aggregates localize to SRRM2-positive nuclear splicing speckles in cell and mouse models of tauopathy.

Multiple nuclear speckle components re-localize to cytoplasmic Tau aggregates

11

236   While examining the co-localization of tau and SRRM2 in nuclear speckles in HEK293

237   cells, we observed that 77% of cytosolic tau aggregates also contained SRRM2 that relocalized to

238   the cytosol (Fig 4A & S4D). Similar results were observed with an SRRM2-halo fusion protein

239   (Fig. S4A). Quantification of SRRM2 IF in cytosolic and nuclear tau aggregates revealed an 11.12-

240   fold and 2.10-fold enrichment over bulk cytosol and nucleoplasm respectively (Fig. S4E). Both

241   the colocalization of nuclear tau aggregates in splicing speckles and the relocalization of SRRM2

242   to cytosolic tau aggregates were independent of the lipofectamine used to transfect tau into the cell

243   models (Fig. S4F).

244

245   The accumulation of SRRM2 into cytosolic Tau aggregates was sufficient to deplete

246   nuclear SRRM2 in HEK293, and an H4 neuroglioma cell line expressing a full length 0N4R P301S

247   tau-YFP that forms fewer nuclear tau aggregates (Fig 4C, 4F). Moreover, we observed SRRM2

248   relocalized into cytoplasmic phospho-tau aggregates in cells without nuclear tau aggregates

249   demonstrating the cytosolic accumulation is independent of nuclear tau aggregates (Fig. 4D).

250   Interestingly, in H4 cells that accumulated SRRM2 in cytosolic tau aggregates, nuclear speckles

251   formed with no change in the intensity of the SON protein, a nuclear speckle protein that does not

252   accumulate in cytosolic tau aggregates (Fig. S4G-H). These observations argue that cytosolic tau

253   aggregates deplete the nucleus of SRRM2, but do not prevent the formation of nuclear speckles.

254

255   To determine if other nuclear speckle proteins also re-localized into cytosolic tau

256   aggregates to some extent, we utilized IF to measure the average intensity enrichment in nuclear

257   and cytosolic tau aggregates. We observed that the SRRM2 paralogs, SRRM1 and SRRM3, did

258   not accumulate in tau aggregates (Fig. 5A, S5A) indicating this accumulation is not shared between

259   SRRM family members. Similarly, proteins with SR domains did not accumulate in cytosolic tau

260   aggregates (SRSF1, SRSF2, and SRSF3) indicating that an SR domain is not sufficient for

261   accumulation in cytoplasmic tau aggregates (Fig. 5A, S5A). Some, but not all, speckle

262   components/splicing factors showed cytosolic tau co-location with PNN (a known binding partner

263   of SRRM2), SFPQ, MSUT2, DDX39B, and DYRK1A showing the strongest enrichment scores

264   (Figure 5A, S5A) (Zimowska et al., 2003). Thus, multiple nuclear speckle proteins involved in

265   pre-mRNA splicing mis-localize to cytosolic tau aggregates with SRRM2, PNN, and SFPQ being

266   the most strongly re-localized.

267

268   Since neither SR domains nor the N-terminal conserved features of SRRM proteins

269   appeared sufficient to recruit proteins to tau aggregates, we hypothesized that the C-terminal

270   domain of SRRM2, which is comprised of an intrinsically disordered region (IDR) (Fig. S5B),

271   might be responsible for SRRM2 recruitment to tau aggregates. This would be consistent with the

272   trend that intrinsically disordered regions of proteins can promote their recruitment to

273   membraneless organelles. To test this idea, we used the CRISPaint system to create two HEK293

274   tau biosensor cell lines that contained a halo tag inserted into endogenous SRRM2 (Ilik et al.,

275   2020; Schmid-Burgk et al., 2016). These two cell lines were 1) a full length SRRM2 cell line

276   referred to as SRRM2_FL-halo (insert at aa 2708), and 2) a cell line lacking the C-terminal IDR

277   of SRRM2 referred to as SRRM2_dIDR-halo (insert at aa 430) (Fig. 5C, S5B-D). We induced tau

278   aggregation in these cells and compared the average SRRM2 halo intensity within nuclear and

279   cytosolic tau aggregates relative to the average intensity in the bulk nucleus or cytosol respectively.

280

281   We observed that SRRM2_FL-halo was recruited to tau aggregates, but that the SRRM2_

282   dIDR-halo was not (Figures 5C-E). This demonstrated that SRRM2 is recruited to tau aggregates

283   by the disordered C-terminal domain rather than the structured N-terminal domain. Since the N-

284   terminal domain of SRRM2 is sufficient for RNA binding and interactions with the core of the

285   spliceosome (Grainger et al., 2009; Zhang et al., 2018), this result argues that SRRM2 is not

286   recruited to cytosolic tau aggregates by binding RNA nor the core of the spliceosome.

287

288   **Tau aggregates alter the properties of nuclear speckles including pre-mRNA splicing**

289   Since cytoplasmic tau aggregates depleted some nuclear speckle components, and tau

290   aggregates can also form in nuclear speckles, we hypothesized that tau aggregate formation might

291   alter the properties and function of nuclear speckles, which we examined in three experiments.

292   First, given that nuclear speckles are highly dynamic structures (Rino et al., 2007) yet the tau

293   aggregating in speckles was essentially static (Fig S1C), we examined if speckles with tau

294   aggregates showed altered dynamics by performing FRAP on two tagged components of speckles,

295   SRRM2 (Halo) and SRSF2 (mCherry). We observed that in the presence of tau aggregates, both

296   speckle components showed an increase in the static component, and a reduced rate of recovery

297   from FRAP (Fig 6A-B). This demonstrates that the presence of Tau aggregates in nuclear speckles

298   changes their dynamics.

299

300   Second, the formation of tau aggregates in speckles alters the organization of speckle

301   components. IF for SRRM2 and SON [a speckle protein that does not relocalize to cytosolic tau

302   aggregates (Fig. 5A)] showed that the two proteins colocalize in speckles in the absence of tau

303   aggregates. However, in the presence of nuclear tau aggregates, SRRM2 and tau colocalize in the

304 center of speckles, while SON moves to the periphery and forms a ring-like structure around the

305 aggregate (Fig. 6C). MSUT2, another protein that shows little relocalization to cytosolic tau

306 aggregates, displayed a similar redistribution from the center of speckles to the periphery in the

307 presence of tau aggregates. Interestingly, knockdown of MSUT2 has been shown to suppress tau

308 toxicity in several model systems (Guthrie et al., 2011; Wheeler et al., 2019), suggesting that tau

309 aggregates disrupt the spatial organization of speckles.

310

311 Third, since nuclear speckles are thought to modulate pre-mRNA splicing (Spector and

312 Lamond, 2011), we performed RNA-Seq on the same HEK293 cells with and without tau

313 aggregates to determine if the presence of tau aggregates could alter splicing. We then investigated

314 splicing patterns using two analyses: MAJIQ and iREADs (Li et al., 2020; Vaquero-Garcia et al.,

315 2016). Specifically, we observed using MAJIQ, at a ΔPSI threshold of 0.1 and confidence

316 threshold of 0.95, we identified 305 local splicing variations in 226 genes that are differentially

317 spliced (Supplemental Table 4). Examination of the types of local splicing variations revealed that

318 the largest categories were intron retention (42.86%), alternative first exons (15.25%), and

319 alternative last exons (11.78%) (Fig 6E MAJIQ splicing diagrams and IGV raw read counts for

320 one example, ATF3, are provided in Fig. S6A-B). Due to the abundance of intron retention events,

321 we used iREAD (intron REtention Analysis and Detector) to better quantify differential intron

322 retention between cells with and without tau aggregates. Reads that fully or partially overlap

323 annotated introns were then used for differential expression analysis using DEseq2 (Li et al., 2020)

324 (Love et al., 2014). We found that at a Padj < 0.05 there were 1,225 introns in 641 genes that were

325 retained in cells with tau aggregates and 120 introns in 86 genes that were retained in cells without

326 tau aggregates (Fig. 6F). Pre-mRNAs with retained introns in cells with tau aggregates cluster in

327 genes affecting apoptosis and splicing associated protein (ASAP) complex, ribosome, and RNA

15

328 splicing and processing (Fig. S6C). Thus, the formation of tau aggregates in cells is sufficient to

329 induce changes in pre-mRNA splicing and is expected to have significant biological impact. Since

330 patients with tauopathies and model systems with tau mutations show changes in pre-mRNA

331 splicing patterns in the brain (Apicco et al., 2019; Hsieh et al., 2019; Raj et al., 2018), an alteration

332 in splicing due to tau aggregate formation may contribute to these splicing changes (see

333 discussion).

334

335 **SRRM2 is depleted from the nucleus and relocalized to cytosolic tau neurofibrillary tangles**

336 **in mouse and human tauopathies**

337 Since SRRM2 was the most highly enriched protein identified, we examined whether

338 cytosolic tau aggregates also contain SRRM2 in mice via IF, using the SC35 antibody on brains

339 from WT B6/J mice, or the Tg2541 mice. In B6 control mice, SRRM2 predominantly localized to

340 poly(A)+ nuclear splicing speckles (Fig. S7A). In contrast, we observe SRRM2 re-localized from

341 the nucleus into cytosolic phospho-tau aggregates in the P301S-expressing Tg2541 mice (Fig.

342 S7A). Consistent with these observations, phosphorylated SRRM2 has been previously observed

343 to be relocalized to the cytosol in 5X FAD mouse brains, however the association of SRRM2 with

344 tau aggregates was not reported (Tanaka et al., 2018). Thus, SRRM2, and potentially other speckle

345 components, relocalize and sequestered into cytosolic tau aggregates in both cell culture models

346 and in tauopathy mice.

347

348 To examine if SRRM2 is mis-localized in human tauopathies, we performed IF on

349 tauopathy patient brains. We observed that in patients with the primary tauopathy CBD, SRRM2

350 was present in tau-containing cytosolic aggregates in the form of neuropil threads, whereas

351   SRRM2 localized to nuclear splicing speckles in aged-matched heathy control patients (Figure 7A,

352   patient demographics in Supplemental Table 3). Quantification of CBD and age matched control

353   images revealed that the average nuclear SRRM2 signal was significantly lower in the CBD brains

354   compared to the controls (Fig 7B). We also observed that SRRM2 was re-localized from the

355   nucleus into the cytosol in the frontal cortex of multiple AD and FTLD patient brains (n=4 AD

356   and n=4 FTLD), but not age-matched control brains (n=4, Figure 7C, S7B, patient demographics

357   in Supp. Table 3). These results show that cytosolic SRRM2 marked by the SC35 antibody is a

358   histopathological feature seen across three distinct human tauopathies.

359

360   **DISCUSSION**

361   We present several lines of evidence that both cytosolic and nuclear tau aggregates contain

362   RNA. First, in mice and HEK293 cells, nuclear and cytosolic tau aggregates both stained positive

363   for poly(A) RNAs, indicating the presence of mRNAs or non-coding RNAs with poly(A) tails

364   (Fig. 1, S1D-E, S7A). Second, purification and sequencing of tau aggregates from mouse brains

365   or HEK293 cells demonstrated the presence and enrichment of specific RNAs, most notably

366   snRNAs and snoRNAs (Fig. 2). Third, FISH for specific RNAs in HEK293 cells validated that our

367   sequencing identified RNAs enriched in tau aggregates (Fig. 3). Although we have not yet

368   examined the specific RNAs present in tau aggregates in human pathologies, tau aggregates in

369   patient brains stain positive with acridine orange, a dye with specificity for RNA (Ginsberg et al.,

370   1997, 1998). Based on these observations, we suggest that tau aggregates generally contain RNA,

371   and the presence of specific RNA species may alter their formation and stability. The presence of

372   RNA in tau aggregates may explain why tau aggregates and other RNA binding proteins can co-

17

373   immunoprecipitate and/or co-localize (Apicco et al., 2018; Gunawardana et al., 2015; Hales et al.,

374   2014a, 2014b; Maziuk et al., 2018; Meier et al., 2016; Vanderweyde et al., 2016).

375

376   We observed that tau aggregates are enriched for a number of different RNA species. Most

377   notably, we observed enrichment of specific snRNA and snoRNAs in both HEK293 reporter cells

378   and in mouse brains, although the specific snRNA/snoRNA species can vary between model

379   systems (Fig. 2). We also observed the enrichment of repetitive RNAs (such as tRNAs, Alu

380   elements, and satellite RNAs) and some mRNAs coding for proteins in the centrosome and

381   spliceosome (Fig. S2D-L). As our library preparation protocol was not specifically designed to

382   capture tRNAs, miRNAs, or rRNAs, our analyses may underestimate the abundance of these

383   species (Motameny et al., 2010; Xu et al., 2019). The mechanisms by which specific RNAs are

384   enriched in tau aggregates remains to be determined but could be due to tau's intrinsic RNA

385   binding specificity, the structure of the tau conformers, and/or the presence of specific RNAs at

386   sites of tau aggregation such as snRNAs in nuclear speckles or mRNAs at the centrosome

387   (Sepulveda et al., 2018). We suggest tau aggregates in cells could be considered a representative

388   of the growing class of RNA and protein assemblies.

389

390   We provide evidence that nuclear tau aggregates form in splicing speckles and alter their

391   properties, composition, and function. One critical observation is that nuclear tau assemblies are

392   observed both in HEK293 cells and P301L mice that overlap with both protein and RNA markers

393   of nuclear speckles (Fig. 4, S4, S7). Moreover, nuclear speckles that contain tau aggregates show

394   altered dynamics of both SRRM2 and SRSF2 (Fig. 6A) demonstrating tau aggregation has altered

395   their material properties. Moreover, tau accumulation in speckles also changes their organization

18

396   with proteins partitioning into novel sub-domains of the assembly (Fig. 6C-D). Finally, since

397   cytoplasmic tau aggregates accumulate multiple components of nuclear speckles, leading to their

398   depletion from the nucleus, the presence of tau aggregates within cells alters the composition of

399   nuclear speckles.

400

401   A critical question is the biological significance of the nuclear tau aggregates. In this light

402   it is important to note we observed tau aggregates in both cell and mouse models of tauopathies

403   demonstrating nuclear tau aggregates are not an artifact of cell line models (Fig. 1C, S1E, S7A).

404   Moreover, we observe tau aggregates in nuclear speckles in both HEK293 cells expressing just the

405   4 repeat regions of tau, and in H4 neuroglioma cells expressing a full-length tau isoform (Fig.

406   S1A) demonstrating tau accumulating in speckles is not an artifact of expressing truncated tau.

407   Although tau is predominantly thought to be a cytosolic microtubule associated protein, numerous

408   labs have observed aggregated and unaggregated tau in the nucleus of neuronal and non-neuronal

409   cells (Bukar Maina et al., 2016; Gärtner et al., 1998; Gil et al., 2017; Jiang et al., 2019; Liu and

410   Götz, 2013; Maj et al., 2010; Montalbano et al., 2020; Rady et al., 1995; Siano et al., 2019; Ulrich

411   et al., 2018; Violet et al., 2014, 2015). Indeed, previous studies in HEK293 cells found that

412   transfection of tau conformers that produced nuclear tau aggregates with a "speckled" phenotype

413   were associated with greater cellular toxicity relative to those that only produced cytosolic tau

414   aggregates (Sanders et al., 2014). In agreement, the suppressor of tau toxicity, MSUT2 (Guthrie et

415   al., 2011; Wheeler et al., 2019), also localized to nuclear splicing speckles (Fig. 6D, S5A). Thus,

416   tau's interaction with splicing speckle components could be integral to the toxicity of tau

417   aggregation.

418

419   A striking feature of our results is that cytoplasmic tau aggregates accumulate and mis-

420   localize several proteins that normally accumulate in nuclear speckles (Fig. 4-6, S4-S7). The most

421   striking of these is the SRRM2 protein, which can show an order of magnitude enrichment in

422   cytosolic tau aggregates as compared to the bulk cytosol (Fig. 5A, S4E). Moreover, we also

423   observed accumulation of SRRM2 in tau aggregates in mice, and in the human tauopathy, CBD

424   (Figure 7A). Strikingly, we observed cytosolic mis-localization and/or nuclear depletion of

425   SRRM2 in multiple tauopathies, including AD and FTLD (Fig. 7C, S7B). The consistent mis-

426   localization of SRRM2 in cell line and animal models of tauopathy, as well as in deceased patient

427   brain samples, argues the mis-localization of nuclear speckle proteins into cytosolic tau aggregates

428   is a fundamental and consistent consequence of tau aggregation. An important issue in future work

429   is to determine the mechanism of nuclear speckle component mis-localization and its biological

430   consequences.

431

432   One likely consequence of altering the composition and dynamics of nuclear speckles

433   would be to alter pre-mRNA splicing. It is well documented that pre-mRNA splicing is altered in

434   tauopathy patient brains, including AD patients (Hsieh et al., 2019; Raj et al., 2018). Consistent

435   with this finding, we demonstrate that the formation of tau aggregates in HEK293 cells is sufficient

436   to induce alterations in alternative splicing and increase the number of significantly retained

437   introns (Fig. 6E, S6). Thus, tau aggregates are sufficient to alter pre-mRNA splicing, although it

438   should be noted that splicing alterations seen in disease tissue may be complicated by additional

439   factors including multiple cell types and neuroinflammatory responses. Interestingly, many of

440   these retained introns triggered by tau aggregates are in RNAs that code for proteins involved in

441   RNA processing and ribosome biogenesis (Fig. S6A). Disruptions to these processes could lead to

442   a pathologic cascade, potentially explaining the complex alterations in ribosome function and RNA

443   processing that have been observed in AD patients (Hsieh et al., 2019; Q et al., 2005; Raj et al.,

444   2018). These results raise the possibility that tau aggregation per se is responsible for some of the

445   splicing changes seen in disease tissue.

446

447   The coaggregation of RNA and proteins in tauopathies is reminiscent of pathologic RNA-

448   protein aggregates seen in other neurodegenerative and neuromuscular diseases, such as

449   amyotrophic lateral sclerosis and inclusion body myopathy (Ramaswami et al., 2013; Taylor et al.,

450   2016). Thus, the sequestration of RNAs and RNA binding proteins into pathologic aggregates may

451   represent a shared pathophysiological feature across multiple degenerative diseases affecting

452   diverse tissue types with a common feature being depletion of critical RNA processing factors

453   from the nucleus leading to changes in RNA processing and gene expression.

454

455   **FIGURE LEGENDS:**

456   **Figure 1: Tau biosensor cell schematic and tau aggregates in mice contain poly(A) RNA.**

457   Tau aggregates in HEK293 biosensor cells and mouse brain contain poly(A) RNA. **(A)**

458   Schematic showing experimental design of tau seeding in HEK293 biosensor cells. Brain

459   homogenate from mice expressing either WT (rTg21221) or P301S (rTg2541) 0N4R tau was

460   homogenized, clarified by successive centrifugation and transfected into HEK293 cells

461   expressing tau K18 (4R repeat domain) tagged with either CFP or YFP. Only cells transfected

462   with P301S homogenate formed bright fluorescent aggregates. **(B)** Tau aggregates form in both

463   the nucleus and the cytosol following transfection of P301S tau homogenate. **(C)** Cytosolic and

464   nuclear tau aggregates contain poly(A) RNA in mouse brain. White pixels in Coloc image show

465   pixels above the Costes determined thresholds in 2D intensity plots (PCC = Pearson correlation

466   coefficient and tM1= thresholded manders colocalization (% of tau pixels above threshold that

467   colocalize with poly(A) pixels above threshold)). X-axis rotation shows AT8 and oligo(dT)

468   staining within the nucleus of mouse Tg2541 cells.

469

470   **Figure 2: The RNA composition of tau aggregates in cellular and mouse tauopathy model**

471   **systems.** The RNA composition of tau aggregates in cellular and mouse tauopathy model

472   systems. **(A)** Scatter plot of RNA sequencing showing average FPKM of two replicates for tau

473   aggregate associated RNA and total RNA. Genes in red are two-fold enriched in tau aggregates

474   and genes in blue are two-fold depleted from tau aggregates. Genes with fewer than 5 FPKM

475   were removed from the analysis due to low coverage. **(B)** Fold change in the percentage of total

476   FPKM for each gene type between the tau aggregate RNA and total RNA. Percentage of total

477   FPKM was calculated by grouping genes using the Ensembl GRCh38.p13 biomart gene types.

478   **(C)** Scatter plot of RNA sequencing data from mouse brain tau aggregate isolation in P301L and

479   WT mice. Enrichment scores were calculated by dividing the insoluble tau IP FPKM by the total

480   RNA FPKM for each replicate. Genes in red are two-fold enriched and genes in blue are two-

481   fold depleted from the P301L sarkosyl insoluble tau aggregates. **(D)** Gene type enrichment in the

482   P301L and WT samples. Fold change for each gene type was calculated by dividing the

483   percentage of total FPKM made up by each gene type in the insoluble tau-IP by the percentage

484   of total FPKM made up by each gene type in the total RNA. The numbers below the gene type

485   names indicate the P301L/WT enrichment.

486

487   **Figure 3: FISH for RNAs in HEK293 tau biosensor cells identified by sequencing.** Line

488   intensity plots and intensity quantification show enrichment of snoRD3A **(A)** and U2 snRNA **(B)**

489   in both the nucleus and cytosol. We observed no enrichment of the depleted mRNA, NUCKS1

490   **(C)**, into nuclear or cytosolic tau aggregates. Bar graphs show quantification of FISH

491   fluorescence intensity within nuclear and cytosolic tau aggregates in relation to bulk cytosol and

492   nucleoplasm (n = 20 aggregates). Significance was determined using an unpaired two-tailed t-

493   test. White pixels in Coloc image show pixels above the Costes determined thresholds in 2D

494   intensity plots (PCC = Pearson correlation coefficient and tM1= thresholded manders

495   colocalization (% of tau pixels above threshold that colocalize with red pixels above threshold)).

496

497   **Figure 4: Tau aggregates colocalize with splicing speckles and mislocalize SRRM2 in**

498   **tauopathy model systems. (A)** Nuclear tau aggregates in HEK293 cells colocalize with SRRM2

499   (SC-35 antibody), a marker of splicing speckles. **(B)** Colocalization analysis showing the

500   relationship between various tau aggregates and SRRM2 **1)** nuclear tau aggregates and splicing

23

501 speckles marked by SRRM2, **2)** a cytosolic tau aggregates that colocalize with cytosolic

502 SRRM2, and **3)** a cytosolic tau aggregate that does not colocalize with SRRM2. **(C)**

503 Quantification of the percent of total SRRM2 intensity in the nucleus in HEK293 cells with and

504 without tau aggregates (n = 23 cells). **(D)** Immunofluorescence of phospho-tau (Thr205) and

505 SRRM2 in H4 neuronal cells expressing 0N4R*P301S-YFP tau +/- tau aggregates shows

506 SRRM2 recruitment to tau aggregates is not dependent on phosphorylation at Thr205. **(E)** 2D

507 intensity plot for the zoomed images showing two Thr205 positive tau aggregates, one that

508 colocalizes with SRRM2 and one that does not colocalize with SRRM2. White pixels in Coloc

509 image show pixels above the Costes determined thresholds in 2D intensity plot. **(F)**

510 Quantification of percentage of SRRM2 in the nucleus in cells with and without tau aggregates

511 (n = 25 cells). Images were quantified using CellProfiler and P-values were calculated using an

512 unpaired two tailed t-test.

513

514 **Figure 5: Other proteins that localize to tau aggregates and the C-terminal region of**

515 **SRRM2 is responsible for localization to tau aggregates. (A, B)** Cytosolic and Nuclear tau

516 aggregates enrichment scores (Median intensity within tau aggregate/median intensity within

517 cytosol or nucleus) for 20 proteins. Ilastik was used to segment images into the following

518 categories: tau aggregates, nucleus, cytosol, and background. Segmentation masks were fed into

519 CellProfiler to quantify the median intensity of the interrogated protein. N=25 images per

520 condition, scale bar represents 95% confidence interval. **(C)** Images of cells CRISPR edited to

521 express endogenous FL or dIDR SRRM2 tagged with halo. **(D)** schematic of SRRM2 constructs.

522 **(E, F)** Cytosolic and nuclear enrichment scores for FL-Halo, dIDR-Halo, and unedited SRRM2.

523

24

524

525   **Figure 6: Tau aggregation alters dynamics and organization of splicing speckles and RNA**

526   **splicing. (A)** FRAP of SRRM2_FL-halo and **(B)** SRSF2-mCherry splicing speckles with and

527   without tau aggregates (n=5). 405 nm laser was used to photobleach and fluorescence intensity

528   was measured using the 647 nm channel for halo-JF647 and 561 nm for mCherry. **(C, D)** Images

529   of P301S tau transfected cells showing nuclear speckle reorganization in the presence of

530   aggregates. SON and MSUT2 move to the periphery of speckles, while SRRM2 remains in the

531   center of speckles with the tau aggregate. **(E)** MAJIQ Analysis of splicing changes in cells with

532   and without tau aggregates showing that most splicing changes are intron retention events. **(F)**

533   Volcano plot showing differential intron retention in cells with tau aggregates quantified by

534   iREAD and DEseq2 (Red = Padj < 0.05). Multiple points per gene are due to the multiple

535   retained introns in those genes.

536

537   **Figure 7: SRRM2 is relocalized to cytosolic tau aggregates in human tauopathies (A)** IF

538   and colocalization analysis showing hyperphosphorylated tau (pTau-Thr205) colocalizes with

539   SRRM2 (SC35) in the cytosol of CBD patient brain while SRRM2 is localized to the nucleus in

540   age matched control brain. **(B)** Quantification of the average nuclear SRRM2 intensity showing a

541   significant decrease in the setting of CBD relative to age matched control. Error bars are 95%

542   confidence interval and p-values were calculated using an unpaired two tailed t-test.

543   Immunohistochemisty of SRRM2 in human brains showing SRRM2 redistribution to the cytosol

544   in AD and FTD brains but retains nuclear localization in control brains. Patient demographics

545   and additional examples can be found in Fig. S5D Table S3.

546

547

SUPPLEMENTAL FIGURE LEGENDS

Supplemental Movies 1, 2, 3: 3D rotation of a HEK293 cell nucleus expressing K18-YFP tau

(1) and a mouse brain nucleus **(2)** showing intranuclear tau aggregates (green) (YFP tagged tau

in HEK293 cells, and AT8 IF in mouse brain) that colocalize with poly(A) signal (red) in

splicing speckles. **(3)** 3D rotation of an H4 cells expressing 0N4R tau-YFP showing intranuclear

tau aggregates.

554

555

Supplemental figure 1: FRAP of nuclear and cytosolic tau aggregates in HEK293 tau

biosensor cells and additional examples of tau aggregates containing poly(A) RNA. (A) H4

neuroglioma cells expressing 0N4R tau-YFP that contain nuclear tau aggregates. **(B, C)** FRAP of

nuclear and cytosolic tau aggregates in HEK293 cells. 405 nm laser was used to photobleach and

fluorescence intensity was measured in the 488cm channel (n=5). Arrow in example images

shows bleached area. **(D)** FISH for Poly(A) RNA in HEK293 cell nuclear and cytosolic tau

aggregates**.** Bar graphs show quantification of poly(A) RNA fluorescence intensity within

nuclear and cytosolic tau aggregates in relation to bulk cytosol and nucleoplasm (n = 35

aggregates). White pixels in Coloc image show pixels above the Costes determined thresholds in

2D intensity plots (PCC = Pearson correlation coefficient and tM1= thresholded manders

colocalization (% of tau pixels above threshold that colocalize with poly(A) pixels above

threshold)). Error bars represent 95% confidence intervals and significance was determined using

an unpaired two-tailed t-test. **(E)** Additional examples from B6 non transgenic and P301S mice

26

569   (Tg2541) showing cytosolic tau aggregates (Ex. 1) and nuclear tau aggregates (Ex. 2, 3) contain

570   RNA.

571

572   **Supplemental figure 2: Additional data on HEK293 and mouse brain tau aggregate**

573   **isolation. (A)** Schematic showing isolation of HEK293 tau aggregates. HEK293 cells transfected

574   with either WT or P301S mouse brain homogenate were lysed, and the cell lysate was stained

575   with the RNA dye, SYTO17, showing the presence of RNA. The cell lysate was then run

576   through a fluorescence activated particle sorter and gates were set to sort fluorescent particles in

577   the P301S but not WT sample. Sorted fractions were examined by fluorescence microscopy to

578   ensure particles were sorted. **(B)** Agilent Tapestation traces and QuBit readings of RNA isolated

579   from sorted tau aggregates. **(C)** Flowcytometry scatter plots showing fluorescence and side

580   scatter of particles for each replicate from the WT and P301S cell lysate (left column). The

581   sorted and waste fractions were then re-run through the flow cytometer to ensure the particles

582   were being sorted (right column). **(D)** Analysis of mRNAs two-fold enriched in tau aggregates

583   from HEK293 cells. Genes from the following groups were highlighted: Voltage-gated calcium

584   channel proteins, histone proteins, centrosomal proteins, and splicing related proteins. **(E)**

585   Cellular component gene ontology of the mRNAs that are two-fold enriched in tau aggregates.

586   **(F, G)** Analysis of multicopy gene families using RepEnrich showing enrichment of specific

587   snoRNA repeats (U8, U17, and U3), snRNA repeats (U1 and U2), tRNA species, and Alu

588   elements. The gene family color scheme is shared between F and G. **(H)** Schematic of tau

589   aggregate isolation from mouse brain. Fractions that were taken for RNA isolation and

590   sequencing are highlighted in Red. **(I)** Western blot of fractions from tau aggregate isolation

591   showing P2 fraction (sarkosyl insoluble fraction) enriches for insoluble tau that is present in the

27

592   P301L mice and not the WT mice. **(J)** Gene type enrichment in the P301L and WT sarkosyl

593   insoluble samples. Fold change for each gene type was calculated by dividing the percentage of

594   total FPKM made up by each gene type in the sarkosyl insoluble fraction (P2) by the percentage

595   of total FPKM made up by each gene type in the total RNA. The numbers below the gene type

596   names indicate the P301L/WT enrichment. Note the absence of snRNA enrichment in the

597   sarkosyl insoluble fraction. **(K)** Mouse vs HEK293 gene type enrichment. **(L)** Scatter plot of

598   mRNA enrichment in mouse brain tau aggregates in P301L and WT mice. Enrichment scores

599   were calculated by dividing the insoluble tau IP FPKM by the total RNA FPKM for each

600   replicate. mRNAs in red are two-fold enriched and mRNAs in blue are two-fold depleted from

601   the P301L sarkosyl insoluble tau IP. Genes with fewer than 5 FPKM were removed from

602   analysis due to low coverage. Two groups of mRNAs were highlighted: centrosomal proteins

603   and splicing related mRNAs.

604

605   **Supplemental figure 3: Additional FISH for RNAs in HEK293 tau biosensor cells. (A, B)**

606   FISH of the enriched RNU6ATAC and snoRA73B shows overlapping fluorescence intensity in

607   nuclear tau aggregates. **(C)** FISH for enriched multicopy Alu RNAs. Quantification shows

608   enrichment in to nuclear and cytosolic tau aggregates, with greater enrichment into cytosolic tau

609   aggregates relative to nuclear aggregates. Bar graphs show quantification of FISH fluorescence

610   intensity within nuclear and cytosolic tau aggregates in relation to bulk cytosol and nucleoplasm

611   (n = 20 aggregates). Significance was determined using an unpaired two-tailed t-test. White

612   pixels in Coloc images show pixels above the Costes determined thresholds in 2D intensity plots

613   (PCC = Pearson correlation coefficient and tM1= thresholded manders colocalization (% of tau

614   pixels above threshold that colocalize with Alu FISH pixels above threshold)). **(D)** FISH for the

615   depleted mRNA, CENPQ, reveals lack of enrichment in nuclear and cytosolic tau aggregates.

616

617

618   **Supplemental figure 4: Additional HEK293 tau biosensor cell data supplementing figure 5.**

619   **(A)** Images of HEK293 biosensor cells expressing SRRM2_FL-halo showing colocalization

620   between nuclear and cytosolic tau aggregates. White pixels in Coloc images show pixels above

621   the Costes determined thresholds in 2D intensity plots (PCC = Pearson correlation coefficient

622   and tM1= thresholded manders colocalization (% of tau pixels above threshold that colocalize

623   with SRRM2_FL-halo pixels above threshold)). **(B, C)** IF for two nucleolar proteins, Fibrillarin

624   and RPF1, showing lack of colocalization between tau aggregates and the nucleolus. Costes

625   method was unable to identify a positive correlation to determine thresholds. **(D)** Analysis of the

626   % of cytosolic tau aggregates that colocalize with SRRM2 in HEK293 tau biosensor cells. 165

627   cells in 5 images were scored by hand as either colocalized or not colocalized. **(E)** Analysis of

628   SRRM2 fluorescence intensity within cytosolic and nuclear tau aggregates relative to bulk

629   cytosol and nucleoplasm (n = 20 measurements). Significance was determined using an unpaired

630   two-tailed t-test. **(F)** Tau aggregates form in both the nucleus and the cytosol with and without

631   lipofectamine 2000 as a transfection reagent showing that SRRM2 mislocalization to cytosolic

632   tau aggregates is not dependent on lipofectamine. **(G, H)** Analysis of whether SRRM2

633   mislocalization disrupts the formation of SON positive splicing speckles. Cells outlined in white

634   are cells that have SRRM2 mislocalized to the cytosol and by visual inspection and

635   quantification of the average SON intensity, have no change in splicing speckles due to the

636   mislocalization of SRRM2. Error bare represent 95% confidence intervals.

637

638   **Supplemental Figure 5: Additional data to support Fig. 5. (A)** Images of proteins examined

639   for their association with tau aggregates in Fig 5 A, B. **(B)** Disorder prediction of SRRM2 by

640   IUPred2 showing the relative ordered nature of the N-terminus and the disorder of the C-

641   terminus. The cwf21domain and the location of the SRRM2_ dIDR-halo truncation are shown.

642   **(C, D)** Schematic of the halo tagged SRRM2 fusion proteins made using CRISPaint and gel

643   showing JF647 conjugated to halo fusion constructs running at the appropriate sizes

644

645   **Supplemental Figure 6: Additional splicing analysis data from cells with and without tau**

646   **aggregates. (A)** Example of intron retention between exon 8 and 9 in ATF3 identified by

647   MAJIQ at ΔPSI threshold of 0.1 and confidence threshold of 0.95. **(B)** Integrated genome

648   viewer image showing raw read counts for each sequencing replicate. Intron retention can be

649   seen between exon 8 and 9. **(C)** Gene ontology of the genes containing significantly retained

650   introns in cells with tau aggregates (FDR < 0.05).

651

652   **Supplemental figure 7: Additional *in vivo* data from mouse and human tauopathies. (A)** IF

653   and FISH showing p-tau (S422) positive tau aggregates colocalized with SRRM2 (SC-35) and

654   poly(A) RNA in the nucleus of Tg2541 mouse hindbrain. White pixels in Coloc images show

655   pixels above the Costes determined thresholds in 2D intensity plots (PCC = Pearson correlation

656   coefficient and tM1= thresholded manders colocalization (% of tau pixels above threshold that

657   colocalize with red pixels above threshold)). Y-axis rotation shows that the pTau(S422) foci

658   being interrogated in the zoomed images are within the nucleus rather than above or below the

659   nucleus. **(B)** IHC in human brain showing cytosolic inclusions of SRRM2 in AD and FTLD

660   patient brains, but not in control brains. (Patient demographics for this figure and Figure 6B can

661   be viewed in Supplemental Table 3).

662

663

664

665

METHODS

Tauopathy mouse models

Animals were maintained in a facility accredited by the Association for Assessment and

Accreditation of Laboratory Animal Care in accord with the Guide for the Care and Use of

Laboratory Animals. All procedures were approved by the University of California, San

Francisco, Institutional Animal Care and Use Committee. Animals were maintained under

standard environmental conditions, with a cycle of 12 hours light and 12 hours dark and free

access to food and water.

For tau seeding experiments in HEK293 tau biosensor cells, the following mice were

used: homozygous B6-Tg(Thy1-MAPT*P301S)2541 mice (referred to as Tg2541 or P301S tau

mice in cellular seeding experiments) and FvBB6F1-Tg(Camk2a-tTa),(tetO-MAPT*wt)21221

(referred to as rTg21221 or WT tau mice in cellular seeding experiments). Mice were euthanized

when the P301S tau mice developed spontaneous pathology (6-7 months). Collected brains were

homogenized to 10% (wt/vol) in DPBS, aliquoted, and frozen at -80°C.

For tau isolation and sequencing of tau aggregates, the following mice were used:

FvBB6F1-Tg(Camk2a-tTA)1Mmay, (tet)-tdTomato-Syp/EGFP)1.1Luo/J,(tetO-

MAPT*P301L)4510 (referred to as rTg4510 or P301L mice in sequencing experiments) and

FvBB6F1-Tg(Camk2a-tTa),(tetO-MAPT*wt)21221 (referred to as rTg21221 or WT tau mice in

sequencing experiments).

685   For IF and FISH experiments, the following mice were used: homozygous B6-Tg(Thy1-

686   MAPT*P301S)2541 mice (referred to as Tg2541 or P301S tau mice in IF and FISH experiments)

687   and C57BL/B6 non transgenic mice (referred to as WT in IF and FISH experiments) were used

688   as a control.

689

690   **Clarification of brain homogenate for tau aggregate seeding in HEK293 cells**

691   10% brain homogenate from Tg2541 or WT mice was centrifuged at 500 x g for 5

692   minutes, the supernatant was transferred to a new tube and centrifuged again at 1,000 x g for 5

693   minutes. The supernatant was again transferred to a new tube and the protein concentration was

694   measured using bicinchoninic acid assay (BCA), and diluted in DPBS to 1 mg/mL for

695   transfection into HEK293 tau biosensor cells.

696

697   **PTA precipitation from brain homogenate for tau aggregate seeding in H4 biosensor cells**

698   PTA precipitation of tau aggregates from mouse brain was performed as described

699   (Woerman *et al,* 2016). 10% brain homogenate was incubated in final concentrations of 2%

700   sarkosyl (Sigma, 61747) and 0.5% benzonase (Sigma, E1014-25KU) with constant agitation at

701   37°C for 2 hours. Sodium PTA (Sigma, P6395) was made in ultrapure MilliQ H_2O and the pH

702   was adjusted to 7.0. PTA was added to the samples to a final concentration of 2%, and samples

703   were then incubated shaking at 37°C overnight. The samples were centrifuged at $13,200 \times g$ at

704   room temperature for 30 minutes, and the supernatant was removed. The resulting pellet was

705   resuspended in 2% sarkosyl/PBS and 2% PTA. The sample was again incubated shaking at 37°C

706   for 2 hours before a second centrifugation as above. The supernatant was again removed, and the

707   pellet was resuspended in 1X PBS to 10% of the initial starting volume. This suspension was

708   incubated using 1μL/well with Lipofectamine 2000 and OptiMEM at room temperature for at

709   least 1.5 hours prior to infecting cells.

710

711   **Cell culture and tau seeding of H4 biosensor cells**

712   H4 cells (ATCC, HTB-148) stably expressing the *pIRESpuro3* vector (Clontech)

713   containing a codon-optimized 0N4R MAPT gene with the P301S point mutation and tagged with

714   YFP were cultured in Dulbecco's Modified Eagle's Medium (DMEM) supplemented with 10%

715   fetal bovine serum (FBS) and 0.2% penicillin-streptomycin, and maintained in incubators set to

716   37°C with 5% carbon dioxide. Cells were plated in a 12-well glass-bottomed dish at $1x10^5$

717   cells/well and allowed to settle for a minimum of 2 hours prior to infection with PTA-

718   precipitated tau prions from Tg2541 mouse brain.

719

720   **Cell culture and tau seeding in HEK293 biosensor cells**

721   HEK293 biosensor cells stably expressing the 4R RD of tau with the P301S mutation

722   were purchased from ATCC (CRL-3275) (previously described in (Holmes et al., 2014)). Cells

723   were seeded at 2.5×10^5 cells/mL in 500uL of DMEM with 10% FBS and 0.2% penicillin-

724   streptomycin antibiotics on PDL coated glass coverslips in a 24-well tissue culture treated plate

725   (Corning 3526) and allowed to grow overnight in incubators set to 37°C with 5% carbon dioxide.

726   The next day, 7ug of 1 mg/mL clarified P301L tau or WT tau mouse brain homogenate was

727   mixed with 6uL of Lipofectamine 2000 and brought up to 100uL in PBS and allowed to sit at

728   room temperature for 1.5 hours. The mixture was then added to 300uL of DMEM without FBS

729   or antibiotics and mixed by pipetting. 50uL of this mixture was added to each well of a 24 well

730   plate and allowed to incubate at 37 °C for 24 hours. Tau aggregate formation was monitored

731   using a fluorescence microscope with a 488nm filter.

732

Generation of Lentiviral particles

734   As previously described (Burke et al., 2019), HEK293T cells (T25 Flask at 80%

735 confluence) were co-transfected with 1ug of pLenti-SRSF2-mCherry-blasticydin, 1ug of pVSV-

736 G, 1ug of pRSV-Rev, and 1ug of pMDLg-pRRe using 16uL of lipofectamine 2000. Medium was

737 replaced 6 hours post-transfection. Medium was then collected at 24- and 48-hours post-

738 transfection and filter sterilized with a 0.45-um filter.

739

Generating SRSF2-mCherry cells via lenti-virus

741   HEK293 biosensor cells were seeded in a T-25 flask. When 80% confluent, the cells were

742 incubated for 1 hour with 1mL of SRSF2-mCherry-blasticydin lentiviral particles containing 10-

743 ug of polybrene with periodic rocking. 4mL of normal medium was then added to the flask and

744 incubated for 24 hours. Normal medium was then aspirated and replaced with selective medium

745 containing 10-ug/mL of Blasticidine S hydrochloride (Sigma-Aldrich). Selective medium was

746 changed every three days. After one-week, selective medium was replaced with normal growth

747 medium. Expression of SRSF2-mCherry was confirmed by fluorescence microscopy.

748

Generating halo tagged SRRM2 cells using CRISPaint

750   HEK293 biosensor cells were seeded in a 6 well plate. As previously described (Ilik et

751 al., 2020; Schmid-Burgk et al., 2016) when 80% confluent, cells were transfected with 1 ug of

752 pCRIPaint-HaloTag-PuroR plasmid, 0.5 ug of PX458-CAS9 targeting plasmid, 0.5 ug of of

753 pCAS9-mCherry-Frame_selector plasmid. After 24 hours, cells were selected using 2 ug/mL

754   puromycin for 48 hours to enrich for edited cells. To label the halo constructs, JF646 was added

755   to growth media at 10 nM overnight prior to cell lysis for gel analysis or fixation for imaging.

756

757   **Immunofluorescence (IF) in HEK293 and H4 cells**

758   Cells were fixed in 4% FPA for 10 minutes, washed 3X with DPBS, permeabilized in

759   0.1% Triton X-100 (Fisher BP151-100) for 5 minutes, washed 3x with PBS, and blocked with

760   5% bovine serum albumin (BSA) for 1 hour. Primary antibodies were diluted to desired

761   concentration in 5% BSA and incubated overnight at 4 deg. Slides were washed 3x with DPBS

762   and secondary antibodies were added at appropriate dilution in 5% BSA and allowed to incubate

763   at room temperature for 1 hour. Slides were washed 2x with DPBS and then incubated in DAPI

764   diluted in PBS (1ug/mL) for 5 minutes at RT, washed 1X with DPBS and then mounted on

765   microscope slides with Prolong glass antifade mountant.

766

767   **Fluorescence in-situ hybridization (FISH)**

768   As previously described (Khong et al., 2017) , cells were fixed in 4% PFA for 10

769   minutes, washed 3x with PBS, permeabilized in 70% ethanol for 1 hour at 4 deg. Cells were then

770   incubated in a wash buffer consisting of 2X nuclease free SSC and 10% deionized formamide

771   (Calbiochem 4610) for 5 minutes at room temperature. The FISH probes were diluted to desired

772   concentration in 100uL of hybridization buffer (2X nuclease-free SSC, 10% deionized

773   formamide, 10% dextran sulfate) and spotted onto parafilm in a hybridization chamber (10cm

774   cell culture dish lined with wet paper towels and covered with parafilm). Coverslips were then

775   inverted onto the droplet of hybridization buffer contain the FISH probes and incubated at 37°C

776   overnight. The slides were then transferred back to a 24 well plate and 500uL of 2X nuclease

777 free SSC with 10% deionized formamide was added for 30 minutes at 37°C. Cells were then

778 incubated in DPBS with 1ug/mL DAPI at room temperature for 5 minutes, washed with 2X

779 nuclease free SSC and incubated at room temperature for 5 minutes. Coverslips were mounted

780 on microscope slides with ProLong Glass Antifade Mountant (ThermoFisher, P36980) and

781 allowed to cure overnight at room temperature.

782 minutes.

783

784 **Image analysis**

785 To quantify FISH intensity within nuclear and cytosolic tau aggregates, ImageJ's

786 freehand selection tool was used to draw perimeters around aggregates and in regions of bulk

787 cytosol and nucleus. The average FISH intensity was measured within the selections and used to

788 compare enrichment of RNAs.

789 To quantify the percentage of SRRM2 in the cytosol of cells, CellProfiler was used.

790 Nuclei were identified using object detection with a typical diameter between 50-200 pixels for

791 HEK293 and H4 cells, which were then used as a mask to quantify nuclear and cytosolic

792 SRRM2 intensity. The percentage of total SRRM2 intensity in the cytosol was calculated by

793 dividing the cytosolic SRRM2 intensity by the sum of the nuclear and cytosolic intensities per

794 image.

795 To quantify enrichment scores of various proteins of interest (POIs) in tau aggregates, 25

796 images were taken in a 5x5 panel of each slide using a 40x air objective on a Nikon Spinning

797 Disc Confocal microscope. Ilastik was used to create the following segmentation masks:

798 cytosolic tau aggregates, nuclear tau aggregates, nucleus, cytosol, and background. The RGB

799 images and segmentation masks were fed into CellProfiler, which was used to quantify the

800   average POI intensity within tau aggregates and the average POI intensity within the

801   corresponding compartment. Enrichment was defined as the ratio of POI intensity within the tau

802   aggregate to the POI intensity within the corresponding compartment.

803

804   **Fluorescent labeling of oligonucleotides for FISH**

805   As previously described (Gaspar et al., 2017), DNA oligonucleotides were labeled with

806   ddUTP-Cy5 fluorophores using terminal deoxynucleotidyl transferase (TdT). DNA

807   oligonucleotides were designed to be antisense to the target of interested with the following

808   specifications: 18-22 nucleotides in length and a minimum of 2 nucleotide spacing between

809   probes. 20uM of DNA oligonucleotides were mixed with 120uM of 5-Propargylamino-ddUTP-

810   Cy5, 10 units of TdT, and 1X TdT buffer and incubated at 37°C for 16 hours. Following

811   incubation, oligonucleotides were precipitated in 80% ethanol with 60mM Na-acetate at -80°C

812   for 20 minutes. The oligonucleotides were pelleted by centrifugation at 16,000g for 20 minutes at

813   4°C, washed with 80% ethanol 2x, air dried, and brought up in 20uL of nuclease free H20. If

814   necessary, a further round of purification can be performed with the Zymo Oligo Clean and

815   Concentrate spin-column kit (Zymo D4060). Labeled probe concentration was measured via

816   NanoDrop OneC UV-Vis Spectrophotometer (Thermo Scientific 840-274200).

817

818   **Tau aggregate isolation from HEK293 cells via centrifugation and flow cytometry**

819   HEK293 biosensor cells were grown to 70-80% confluency in 245 mm square tissue

820   culture treated dishes (Corning 07-200-599) in 50mL of DMEM (one plate per biologic

821   replicate). 200 ug of WT or P301S tau clarified mouse brain homogenate was transfected per

822   dish using lipofectamine 2000 and incubated at 37°C for 24 hours. Tau aggregation was

823   monitored using the Evos M500 Imaging System with a GFP filter. Cells were harvested by

824   scraping, centrifuged at 200 rcf, snap frozen in liquid nitrogen, and stored at -80°C.

825   The cell pellet was thawed on ice for 5 minutes and resuspended in 6mL of high salt, high

826   sucrose buffer containing RNase Inhibitors (10mM Tris-HCl pH 7.4, 0.8M NaCl, 1 mM EGTA,

827   10% sucrose, 0.5% NP40, Complete ultra-protease inhibitor, PhosStop Phosphatase inhibitor,

828   1:1500 RNasein, 1:300 Ribolock, 1:60 turbo DNAse). Cell lysate was passed through a 25 G

829   needle 3x to homogenize and 100uL of sample was taken to extract total RNA.

830   Large tau complexes were pelleted by centrifugation at 21,000g for 20 minutes at 4 °C,

831   the pellet was brought up in high salt/high sucrose buffer, passed through a 27G needle, and

832   centrifuged at 10,000g for 10 minutes at 4 °C. The pellet was brought up in 1mL of DPBS and

833   centrifuged at 500g for 5 minutes at 4 °C to pellet large cellular debris. The supernatant (S3,

834   enriched tau fraction) was taken and spotted onto a microscope slide for fluorescent imaging of

835   tau aggregates in solution.

836   A BD Biosciences FACSAria Fusion flow cytometer was used to sort tau aggregates by

837   fluorescence and size. The sheath fluid was changed to PBS, flow rate was set to 1.2, and

838   threshold rate was set to <200 events/second. Gates were set on side scatter-H and 488

839   fluorescence such that WT transfected S3 fractions had <1% of particles in sorted fraction and

840   P301S transfected S3 fractions had >30% in the sorted fraction. Roughly 1 million particles were

841   sorted for each sample. To ensure the flow cytometer was sorting particles properly, the sorted

842   fraction was visually inspected by fluorescence microscopy and the sorted and waste fractions

843   were run back through the flow cytometer.

844   To denature tau aggregates and extract RNA, the sorted fractions were brought up in

845   Proteinase K buffer (2M Urea, 100ug/mL proteinase K, and 3mM DTT) and incubated at room

39

846   temperature for 15 minutes. Guanadinium HCl was added to a final concentration of 5M and

847   incubated at room temperature for 30 minutes. RNA was then extracted with TRIzol LS reagent

848   (ThermoFisher 10296010). RNA concentrations were measured by QuBit RNA HS Assay kit

849   (ThermoFisher Q328521) and Agilent 4200 TapeStation using the High Sensitivity RNA

850   ScreenTape (Agilent 5067-5579). All samples except for the WT transfected sorted fraction

851   yielded sufficient RNA to prepare sequencing libraries (Fig S2B for Tapestation data). RNA

852   sequencing libraries were then prepared from total RNA and tau aggregate associated RNA from

853   HEK293 biosensor cells using the Roche KAPA RNA HyperPrep Kit with RiboErase (Kapa

854   KK8560) and sequenced on an Illumina NextSeq sequencer at the University of Colorado,

855   Boulder BioFrontiers Sequencing Core.

856

857   **Isolation of tau aggregates from mouse brain**

858   Brains were harvested from two Tg21221 (WT 0N4R human tau mouse brains) and two

859   rTg4510 (P301L 0N4R human tau) mice and snap frozen in liquid nitrogen. Samples were

860   thawed on ice and weighed. The brain tissue was then homogenized on ice using a dounce

861   homogenizer and diluted to 5 mL/g in homogenization buffer with RNase inhibitors (10mM

862   Tris-HCl pH7.4, 0.8M NaCl, 1mM EGTA, 10% sucrose, 1X Roche protease inhibitor, 1:40

863   promega RNasein). Aliquots were stored at -80 C.

864   To extract total RNA, 50uL of brain homogenate was incubated for 2 hours at room

865   temperature in proteinase K buffer (2% SDS, 4M Urea, 10mM Tris-HCl pH4.54, 100ug/mL

866   Proteinase K). 400uL of Urea buffer (60mM Tris-HCl pH 8.5, 8M Urea, 2% SDS) was then

867   added and incubated for 30 minutes at room temperature. RNA was extracted from one half of

868   this reaction using TRIzol LS solution and the other half was frozen at -80°C.

869   900uL of frozen brain homogenate was thawed on ice and 100uL of 10% (w/v) sarkosyl

870   solution was added and incubated on ice for 15 minutes. Homogenate was then passed through a

871   25G and 27G syringe. Protein concentrations were measured by QuBit Protein Assay Kit

872   (Thermo Fisher, Q33211) and sarkosyl buffer (50mM HEPES pH 7.2, 250 mM sucrose, 1mM

873   EDTA, 1% w/v sarkosyl, 0.5 M NaCl) was added to reach a final concentration of 10 mg/mL.

874   500uL of each sample was transferred into an untracentrifuge tube (Beckman Coulter, 349623)

875   and centrifuged at 180,000g for 30 min at 4 deg in a Beckman Coulter Optima MAX-XP

876   Ultracentrifuge. The supernatant (S1 fraction) was removed and stored at -80°C. The pellet was

877   then brought up in 500uL of sarkosyl buffer and run through a 25G needle to homogenize. The

878   sample was then centrifuged at 180,000g for 30 min at 4°C and the supernatant (S2) was

879   removed and stored at -80°C.

880   For the sarkosyl insoluble RNA sequencing, P2 pellet was brought up in 100uL of

881   proteinase K buffer and incubated at RT for 2 hours at RT. To further solubilize the sample,

882   400uL of urea buffer was added and incubated at RT for 30 minutes. The sample was then split

883   in two and RNA was extracted from one half (250uL) using Trizol LS solution the other half was

884   frozen at -80°C.

885   For the Tau IP, the P2 fraction was brought up in 400uL of PBS and protein

886   concentrations were measured using the QuBit Protein Assay Kit (Thermo Fisher, Q33211).

887   Samples were precleared with 15mg of DEPC treated (to inactivate RNAse) protein A dynabeads

888   at room temperature for 45 minutes at RT on rotator. While preclearing, Tau12 and IgG

889   antibodies were conjugated to 50uL (1.5mg) of protein A dynabeads for 40 minutes on rotator.

890   Following preclear step, the sample was split into two fractions (one for the Tau12 IP and one for

891   the IgG IP). Dynabeads with conjugated antibody were washed with PBS, brought up in 50uL of

41

892   PBS and added to sample. IP was carried out on rotator at room temperature for 40 minutes.

893   Sample was then washed 3x with PBS and 100uL of proteinase K buffer was added to the beads

894   and incubated at RT for 2 hours. 400uL of urea buffer was added to beads and incubated for 30

895   minutes to further denature. Samples were then split into two 250uL fractions, one was Trizol

896   extracted. RNA concentrations were then measured by QuBit RNA HS Assay kit (ThermoFisher

897   Q328521) and Agilent 4200 TapeStation using the High Sensitivity RNA ScreenTape (Agilent

898   5067-5579). IgG IP did not pull down any RNA. RNA sequencing libraries were prepared using

899   the Nugen Ovation SoLo RNA-Seq System, Mouse (Nugen 0501-32) and sequenced on an

900   Illumina NovaSeq sequencer at the University of Colorado, Anschutz Genomics and Microarray

901   Core.

902

903   **Analysis of RNA sequencing data**

904   Following sequencing, quality of sequencing reads were assessed using FASTQC version

905   0.11.5, Illumina TruSeq3 adapters and low quality reads were trimmed off using Trimmomatic

906   version 0.36 (Bolger et al., 2014). Reads that aligned uniquely to the ribosome, yeast, or bacteria

907   were then filtered out using FastQ Screen (Wingett and Andrews, 2018). Reads were aligned

908   using the Spliced Transcripts Alignment to a Reference (STAR) aligner version 2.6.0 (Dobin et

909   al., 2013) to either the Genome Reference Consortium Human Build 38 (GRCh38, acquired from

910   NCBI) or the Genome Reference Consortium Mouse Build 38 (GRCm38, acquired from NCBI)

911   depending on the species being analyzed. Adjusted p-values were calculated from raw read

912   counts using DEseq2. Gene counts were used to calculate Fragments per kilobase per million

913   read (FPKM) using transcript lengths retrieved from the Ensembl Biomart (Kinsella et al., 2011)

914   and the following formula FPKM = (# of mapped fragments$*10^3*10^6$)/(transcript length in bp $*$

915   total number of mapped fragments). For mouse sequencing, FPKM values were used to calculate

916   enrichment scores for each biological replicate by dividing the Tau IP FPKM by the Total RNA

917   FPKM for each replicate. Enrichment scores were then used to calculate average enrichment

918   score for each gene and fold changes between P301L and WT mice. Gene type enrichment was

919   determined by calculating the percentage of FPKM made up by each gene type. Repetitve

920   elements were analyzed using a reference files acquired from repeatmasker (hg38 - Dec 2013 -

921   RepeatMasker open-4.05 – Repeat Library 20140131) and RepEnrich (Criscione et al., 2014).

922   Splicing analysis: Following mapping of reads to GRCh38 using STAR, MAJIQ v2.1

923   was used with standard settings to quantify splicing changes. Voila was used to view results,

924   generate splicing diagrams, and determine the relative percentage of each splicing type (only

925   LSVs containing more than 10 reads were reported). To quantify reads mapping to introns,

926   iREAD v0.8.5 was used along with an intron annotation file generated from ensemble v77. The

927   read count output from iREAD was used as an input to DEseq2 for calling differential intron

928   retention.

929

930   **Fluorescence recovery after photobleaching**

931   HEK293 biosensor cells were seeded in DMEM supplemented with 10% FBS and 0.2%

932   penicillin-streptomycin at 0.25×10^5 cells/mL in Grenier Bio-One CELLview dishes with Glass

933   Bottoms (Thomas Scientific, 07-000-235) and grown overnight at 37°C. The next day, clarified

934   P301S tau brain homogenate was transfected and grown for 24 hours. A Nikon A1R Laser

935   Scanning Confocal with environmental chamber was used to image the cells. A circular region

936   within a tau aggregate was defined and bleached using a 405nm laser set to 100% laser power.

937   For determining the recovery of tau within tau aggregates (Fig S1B-C), fluorescence intensity

938   was measured continuously for 6 minutes and 30 seconds post bleaching (N=5). For determining

939   the recovery of SRRM2_FL-halo within splicing speckles with and without tau aggregates,

940   fluorescence intensity was measured continuously for 30 seconds (n=5). For determining the

941   recovery of SRSF2-mCherry within splicing speckles with and without tau aggregates,

942   fluorescence intensity was measured every 1 second for 30 seconds (n=5).

943

944

945   **Mouse brain RNA fluorescent *in situ* hybridization followed by immunofluorescent**

946   **staining (RNA FISH-IF)**

947   Control (B6/J) and Tg2541 animals at approximately 6 months of age were anesthetized

948   for whole brain collection. The mouse brains were embedded in OCT compound (Sakura, 4583)

949   and flash-frozen in chilled isopentane. Samples were sectioned at 12μm using a cryostat and

950   mounted on glass slides. Samples were air-dried at room temperature for 20 minutes to ensure

951   tissue adherence to slides, then fixed in cold 4% PFA/1X PBS for 15 minutes. Samples were

952   washed 3 times in 1X PBS for 5 minutes/wash, followed by a wash in 1X SSC for 5 minutes.

953   Samples were transferred into 0.1X citrate buffer (Sigma, C9999) for a gentle antigen retrieval at

954   60°C for 1 hour 15 minutes. The slides were allowed to cool for 15 minutes, then rinsed 3 times

955   in 1X SSC for 5 minutes/wash. Samples were then dehydrated in a graded series of ethanol

956   washes (50%, 70%, 90% and 100%) for 3 minutes/wash and air-dried for 10 minutes. A

957   hydrophobic barrier was drawn around the tissue and samples were blocked in a pre-

958   hybridization buffer of 3% normal goat serum (NGS)/4X SSC at 37°C for 1 hour in a humidified

959   chamber. Oligo(dT) probe labeled with Quasar 570 or Quasar 670 (Stellaris) was added to

960   hybridization buffer (Stellaris, SMF-HB1-10) and incubated at 65°C for 10 minutes followed by

961   a cooling on ice for 2 minutes. Pre-hybridization buffer was removed, and samples were then

962   incubated in probe/hybridization buffer at 37°C overnight.

963   The next day, samples were washed in a dilution series of pre-hybridization buffer (twice

964   in 4X, then once in 2X, 1X, 0.1X) at 37°C for 10 minutes/wash. Samples were then blocked in

965   20% NGS/1X PBST (0.1% Tween-20) at room temperature for 1 hour and incubated at room

966   temperature overnight in primary antibodies diluted at 1:250 in 10% NGS/1X PBST.

967   The next day, samples were washed 3 times in 1X PBST for 10 minutes/wash, then

968   incubated in Alexa Fluor secondary antibodies diluted at 1:500 in 10% NGS/1X PBST for 2

969   hours at room temperature. Samples were washed 3 times in 1X PBST for 10 minutes/wash. To

970   quench autofluorescence, samples were incubated in 0.1% Sudan Black B in 70% ethanol for 10

971   minutes, then rinsed briefly in fresh 70% ethanol and transferred into 1X PBS for 5 minutes.

972   Coverslips were mounted onto the slides using Vectashield Vibrance antifade mounting medium

973   with DAPI (Vector Laboratories H-1800) and slides were left to dry overnight prior to being

974   imaged with a Leica SP8 confocal microscope.

975

976   **Human brain immunofluorescent staining**

977   Human brain samples were provided by the Neurodegenerative Disease Brain Bank at the

978   University of California, San Francisco, which receives funding support from NIH grants

979   P01AG019724 and P50AG023501, the Consortium for Frontotemporal Dementia Research, and

980   the Tau Consortium.

981   Formalin-fixed paraffin-embedded (FFPE) human brain samples from the left angular

982   gyrus region of control individuals and patients diagnosed with corticobasal degeneration (CBD)

983   were sliced at 8μm and mounted on glass slides. Samples were deparaffinized in a 60°C oven

984 overnight, followed by two 10-minute xylene washes. Samples were then rehydrated in a graded

985 series of ethanol washes (twice in 100% then once each in 90%, 70%, 50%) for 3 minutes/wash.

986 Slides were then rinsed in cold ultrapure MilliQ H_2O and transferred into 0.1X citrate buffer

987 (Sigma, C9999) for antigen retrieval in an autoclave at 120°C for 5 minutes. Slides were allowed

988 to cool for 15 minutes, then rinsed in 1X PBST (0.25% Triton X-100) for 15 minutes. A

989 hydrophobic barrier was drawn around the tissue and samples were blocked in 20% normal goat

990 serum (NGS)/1X PBST at room temperature for 1 hour in a humidified chamber. Samples were

991 incubated at room temperature overnight in primary antibodies diluted at 1:250 in 10% NGS/1X

992 PBST.

993 The next day, samples were washed 3 times in 1X PBST for 10 minutes/wash, then

994 incubated in Alexa Fluor secondary antibodies diluted at 1:500 in 10% NGS/1X PBST for 2

995 hours at room temperature. Samples were washed 3 times in 1X PBST for 10 minutes/wash. To

996 quench autofluorescence, samples were incubated in 0.1% Sudan Black B in 70% ethanol for 10

997 minutes, then rinsed briefly in fresh 70% ethanol and transferred into 1X PBS for 5 minutes.

998 Samples were incubated for 10 minutes in 5μg/mL DAPI diluted in 1X PBS, then washed for 10

999 minutes in 1X PBS. Coverslips were mounted onto the slides using Vectashield Vibrance

1000 antifade mounting medium (Vector Laboratories H-1700) and slides were left to dry overnight

1001 prior to being imaged with a Leica SP8 confocal microscope.

1002

1003 **Human tissue samples for immunohistochemistry**

1004 AD, FTD and non-neurologic disease control post-mortem tissue samples were obtained

1005 from the University of Pittsburgh ALS Tissue Bank, the Barrow Neurological Institute ALS

1006 Tissue Bank, and the Target ALS Human Postmortem Tissue Core. All tissues samples were

1007   collected after informed consent from the subjects or by the subjects' next of kin, complying

1008   with all relevant ethical regulations. The protocol and consent process were approved by the

1009   University of Pittsburgh Institutional Review Board (IRB) and the Dignity Health Institutional

1010   Review Board. Clinical diagnoses were made by board certified neuropathologists. Subject

1011   demographics are listed in Supplemental Table 3.

1012

1013   **Immunohistochemistry**

1014   Paraffin-embedded post-mortem frontal cortex tissue sections were used for this study.

1015   All sections were deparaffinized, rehydrated and antigen retrieval performed using Target

1016   Antigen Retrieval Solution, pH 9.0 (DAKO) for 20 min in a steamer. After cooling to room

1017   temperature, non-specific binding sites were blocked using Super Block (Scytek), supplemented

1018   with Avidin (Vector Labs). Primary antibodies used for immunohistochemistry were incubated

1019   overnight in Super Block with Biotin. Slides were then washed and incubated for 1 h in the

1020   appropriate biotinylated IgG secondary antibodies (1:200; Vector Labs) in Super Block. Slides

1021   were washed in PBS and immunostaining visualized using the Vectastain Elite ABC reagent

1022   (Vector Labs) and Vector Immpact NovaRED peroxidase substrate kit (Vector Labs). Slides

1023   were counterstained with hematoxylin (Sigma Aldrich) and pictures were captured using an

1024   OLYMPUS BX40 microscope equipped with a SebaCam camera.

1025   **Antibody information**

Antibody name	Manufacturer	Catalog #
Mouse anti-phospho tau S202, Thr205	Invitrogen	MN1020
Rabbit anti-pTau Thr205	Invitrogen	44-738G
Mouse anti-pTau (Ser202, Thr205) AT8	Invitrogen	MN1020
Mouse anti-SRRM2 (SC-35)	Abcam	Ab11826
Rabbit anti-Pinin	Thermo Scientific	18266-1-AP
Rabbit anti-SFPQ	Abcam	Ab177149
Rabbit anti-ZC3H14 (MSUT2)	Sigma-Aldrich	HPA049798

Rabbit anti-DDX39B	OriGene	TA890032
Rabbit anti-DYRK1A	Abcam	ab65220
Rabbit anti-SRSF2	Abcam	Ab204916
Rabbit anti-SNRNP70 (U1-70K)	Abcam	ab83306
Rabbit anti-PABP	Abcam	ab21060
Rabbit anti-TIA1	Abcam	ab40693
Rabbit anti-SRRM3	Sigma-Aldrich	HPA019337
Rabbit anti-SRSF1 (SF2)	Abcam	ab129108
Mouse anti-G3BP	Abcam	ab56574
Rabbit anti-SNRPA1	Millipore Sigma	HPA045622
Rabbit anti-PQBP1	Millipore Sigma	HPA001880
Rabbit anti-PNISR	Millipore Sigma	HPA038796
Rabbit anti-RPF1	Sigma-Aldrich	HPA024642
Rabbit anti-U2AF1	Sigma-Aldrich	HPA044833
Rabbit anti-SON	Thermo Fisher	PA565108
Rabbit anti-Fibrillarin	Invitrogen	MA1-22000
Goat anti-mouse 647	Abcam	Ab150115
Goat anti-rabbit 647	Abcam	Ab150079

1026

1027 **Fluorescence in-situ hybridization probe information**

Probe name and label	Sequence(s)
Oligo(dT)-Cy5	TTT TTT TTT TTT TTT TTT TTT TTT TTT TTT
Oligo(dT)-Quasar670	TTT TTT TTT TTT TTT TTT TTT TTT TTT TTT
U2 snRNA-Cy5	1: CCAAAAGGCCGAGAAGCGAT 2: ACAGATACTACACTTGATCT 3: CTCGGATAGAGGACGTATCA 4: CCTGCTCCAAAAATCCATTT 5: CGTGGAGTGGACGGAGCAAG 6: TGGAGGTACTGCAATACCAG
RNU6ATAC snRNA-AF647	AAAAAACGATGGTTAGATGCCACG
snoRA73B-AF647	AGCCCTAAGCTCCCCTATGCCAC
snoRD3A-AF647	GCGTTCTCTCCCTCTCACTCCCCAATA
NUCKS1-Cy5	1: GAGAAGCCAAAGACCAGGAC 2: CGACATGTTCGCTGTCGAAA 3: TCTCGGGGAGATGATCGAAT 4: AATCTTTCTCCTGGAATGGT 5: TTCCTTTGATGCCTTTGAAG 6: GCCAAAACCATGTTCTATCT 7: ACTGAAAGCCCATGAGTCAA 8: CCTCATCGGTGGAAGTTTAA 9: ATTCATCTTTATCTCCTACC 10: ACCTGTAGACTGATCTTGTT 11: AGGGCCAGGAAAATAGTGTC 12: CTAGTCAAGGACAGGATGGG

	13: CTGAATTGTATGGGAGCAGC
	14: ACTGCTTTTATAAGGCGTGT
	15: AAACCTACGGATCTATCTCC
	16: CGCCTGGTATTAGATGTGAA
	17: CATACCAGGACCCTTTAAAC
	18: GCCCAATCAAATGCACACAA
	19: GACTATTGAGCACCTGTATC
	20: TCCTGACATCACTATCAAGC
	21: CTTCCTGAGCACTGCAAAAT
	22: AGGTAAACCTAGCAGAGCTA
	23: GAATGTAGTGTCAGTCAGCA
	24: TATGCTACGTATGTCTAGCT
	25: GGAGGACTAAAAGCAGCAGC
	26: TCCCTAAAGGAGGAAACACC
	27: TGTAAGCTCCTTCAAGGGAA
	28: ACTGGGGCAAACAGGTTATT
	29: TCTAGCTGACCATATTCACA
	30: AACGCTCTCAAAGCATCTCG
	31: TCTTTTATAAAGCTTTCCCC
	32: TACATTTTCCCTATCCTATG
	33: TAAGCCAACTCTCCATTTTC
	34: TAGATAGCTTGATGTCCCAA
	35: TTTGTATCGAATTTACCCCA
	36: TCAGCACCACTGTGAATTTT
	37: GTTTCCCAATAGTGGTTATT
	38: GCTCAAACAGATGTCACCAG
	39: ATTCTACCAGCCACACAAAG
	40: AGGGCATAAGCTGAGTACTA
	41: TTGCTGCAACATGTTCATGG
	42: CCTTTCTTTAACCTTGTAGG
	43: AGCCCATGGACTAGTTAATA
	44: CACACGATTCTACCAATGCA
	45: ATCTGGGTTATAAAAGCCCT
	46: CAAAGTCAGGCTGAACTGGG
	47: GGTAAGTCTACTGCTTCTTG
	48: TTTGCTTTCCACAACACTTC
Alu-Cy5	1: GAGACAGGGTCTCGCTCTGT
	2: CCCAGGCTGGAGTGCAGTGG
	3: CGATCATAGCTCACTGCAGC
	4: CGAACTCCTGGGCTCAAGCG
	5: CCTCCTGCCTCAGCCTCCCG
	6: TAGCTGGGACTACAGGCGCG
	7: CCACCACGCCCGGCTAATTT
	8: GTATTTTTTGTAGAGACGGG
	9: CTCGCTATGTTGCCCAGGCT
	10: TCTCGAACTCCTGGGCTCAA

49

	11: GATCCTCCCGCCTCGGCCTC 12: AAAGTGCTGGGATTACAGGC 13: GAGCCACCGCGCCCGGCC

1028

1029

1030

1031 Ambadipudi, S., Biernat, J., Riedel, D., Mandelkow, E., and Zweckstetter, M. (2017). Liquid-liquid
1032 phase separation of the microtubule-binding repeats of the Alzheimer-related protein Tau. Nat
1033 Commun *8*, 275.

1034 Aoyagi, A., Condello, C., Stöhr, J., Yue, W., Rivera, B.M., Lee, J.C., Woerman, A.L., Halliday, G.,
1035 Duinen, S. van, Ingelsson, M., et al. (2019). Aβ and tau prion-like activities decline with longevity
1036 in the Alzheimer's disease human brain. Science Translational Medicine *11*.

1037 Apicco, D.J., Ash, P.E.A., Maziuk, B., LeBlang, C., Medalla, M., Abdullatif, A.A., Ferragud, A.,
1038 Botelho, E., Ballance, H.I., Dhawan, U., et al. (2018). Reducing the RNA binding protein TIA1
1039 protects against tau-mediated neurodegeneration in vivo. Nat Neurosci *21*, 72–80.

1040 Apicco, D.J., Zhang, C., Maziuk, B., Jiang, L., Ballance, H.I., Boudeau, S., Ung, C., Li, H., and
1041 Wolozin, B. (2019). Dysregulation of RNA Splicing in Tauopathies. Cell Rep *29*, 4377-4388.e4.

1042 Bai, B., Hales, C.M., Chen, P.-C., Gozal, Y., Dammer, E.B., Fritz, J.J., Wang, X., Xia, Q., Duong,
1043 D.M., Street, C., et al. (2013). U1 small nuclear ribonucleoprotein complex and RNA splicing
1044 alterations in Alzheimer's disease. PNAS *110*, 16562–16567.

1045 Bolger, A.M., Lohse, M., and Usadel, B. (2014). Trimmomatic: a flexible trimmer for Illumina
1046 sequence data. Bioinformatics *30*, 2114–2120.

1047 Brandt, R., Léger, J., and Lee, G. (1995). Interaction of tau with the neural plasma membrane
1048 mediated by tau's amino-terminal projection domain. J. Cell Biol. *131*, 1327–1340.

1049 Broccolini, A., Engel, W.K., Alvarez, R.B., and Askanas, V. (2000). Paired helical filaments of
1050 inclusion-body myositis muscle contain RNA and survival motor neuron protein. Am. J. Pathol.
1051 *156*, 1151–1155.

1052 Buée, L., Bussière, T., Buée-Scherrer, V., Delacourte, A., and Hof, P.R. (2000). Tau protein
1053 isoforms, phosphorylation and role in neurodegenerative disorders11These authors
1054 contributed equally to this work. Brain Research Reviews *33*, 95–130.

1055 Bukar Maina, M., Al-Hilaly, Y.K., and Serpell, L.C. (2016). Nuclear Tau and Its Potential Role in
1056 Alzheimer's Disease. Biomolecules *6*.

1057 Burke, J.M., Moon, S.L., Matheny, T., and Parker, R. (2019). RNase L Reprograms Translation by
1058 Widespread mRNA Turnover Escaped by Antiviral mRNAs. Mol. Cell *75*, 1203-1217.e5.

1059 Chen, J., Kanai, Y., Cowan, N.J., and Hirokawa, N. (1992). Projection domains of MAP2 and tau
1060 determine spacings between microtubules in dendrites and axons. Nature *360*, 674–677.

1061 Criscione, S.W., Zhang, Y., Thompson, W., Sedivy, J.M., and Neretti, N. (2014). Transcriptional
1062 landscape of repetitive elements in normal and cancer human cells. BMC Genomics *15*, 583.

1063 Delaval, B., and Doxsey, S.J. (2010). Pericentrin in cellular function and disease. J Cell Biol *188*,
1064 181–190.

1065 DeVos, S.L., Corjuc, B.T., Commins, C., Dujardin, S., Bannon, R.N., Corjuc, D., Moore, B.D.,
1066 Bennett, R.E., Jorfi, M., Gonzales, J.A., et al. (2018). Tau reduction in the presence of amyloid-β
1067 prevents tau pathology and neuronal death in vivo. Brain *141*, 2194–2212.

1068 Diner, I., Nguyen, T., and Seyfried, N.T. (2017). Enrichment of Detergent-insoluble Protein
1069 Aggregates from Human Postmortem Brain. J Vis Exp.

1070 Dinkel, P.D., Holden, M.R., Matin, N., and Margittai, M. (2015). RNA Binds to Tau Fibrils and
1071 Sustains Template-Assisted Growth. Biochemistry *54*, 4731–4740.

1072 Dobin, A., Davis, C.A., Schlesinger, F., Drenkow, J., Zaleski, C., Jha, S., Batut, P., Chaisson, M.,
1073 and Gingeras, T.R. (2013). STAR: ultrafast universal RNA-seq aligner. Bioinformatics *29*, 15–21.

1074 Falcon, B., Zhang, W., Murzin, A.G., Murshudov, G., Garringer, H.J., Vidal, R., Crowther, R.A.,
1075 Ghetti, B., Scheres, S.H.W., and Goedert, M. (2018). Structures of filaments from Pick's disease
1076 reveal a novel tau protein fold. Nature *561*, 137–140.

1077 Falcon, B., Zivanov, J., Zhang, W., Murzin, A.G., Garringer, H.J., Vidal, R., Crowther, R.A., Newell,
1078 K.L., Ghetti, B., Goedert, M., et al. (2019). Novel tau filament fold in chronic traumatic
1079 encephalopathy encloses hydrophobic molecules. Nature *568*, 420–423.

1080 Fitzpatrick, A.W.P., Falcon, B., He, S., Murzin, A.G., Murshudov, G., Garringer, H.J., Crowther,
1081 R.A., Ghetti, B., Goedert, M., and Scheres, S.H.W. (2017). Cryo-EM structures of tau filaments
1082 from Alzheimer's disease. Nature *547*, 185–190.

1083 Galganski, L., Urbanek, M.O., and Krzyzosiak, W.J. (2017). Nuclear speckles: molecular
1084 organization, biological function and role in disease. Nucleic Acids Res *45*, 10350–10368.

1085 Gärtner, U., Janke, C., Holzer, M., Vanmechelen, E., and Arendt, T. (1998). Postmortem changes
1086 in the phosphorylation state of tau-protein in the rat brain. Neurobiol. Aging *19*, 535–543.

1087 Gaspar, I., Wippich, F., and Ephrussi, A. (2017). Enzymatic production of single-molecule FISH
1088 and RNA capture probes. RNA *23*, 1582–1591.

1089 Gil, L., Federico, C., Pinedo, F., Bruno, F., Rebolledo, A.B., Montoya, J.J., Olazabal, I.M., Ferrer, I.,
1090 and Saccone, S. (2017). Aging dependent effect of nuclear tau. Brain Research *1677*, 129–137.

1091 Ginsberg, S.D., Crino, P.B., Lee, V.M., Eberwine, J.H., and Trojanowski, J.Q. (1997).
1092 Sequestration of RNA in Alzheimer's disease neurofibrillary tangles and senile plaques. Ann.
1093 Neurol. *41*, 200–209.

1094 Ginsberg, S.D., Galvin, J.E., Chiu, T.S., Lee, V.M., Masliah, E., and Trojanowski, J.Q. (1998). RNA
1095 sequestration to pathological lesions of neurodegenerative diseases. Acta Neuropathol. *96*,
1096 487–494.

1097 Goedert, M. (2005). Tau gene mutations and their effects. Movement Disorders *20*, S45–S52.

1098 Goedert, M., and Spillantini, M.G. (2000). Tau mutations in frontotemporal dementia FTDP-17
1099 and their relevance for Alzheimer's disease. Biochim. Biophys. Acta *1502*, 110–121.

1100 Goedert, M., Wischik, C.M., Crowther, R.A., Walker, J.E., and Klug, A. (1988). Cloning and
1101 sequencing of the cDNA encoding a core protein of the paired helical filament of Alzheimer
1102 disease: identification as the microtubule-associated protein tau. Proc. Natl. Acad. Sci. U.S.A.
1103 *85*, 4051–4055.

1104 Grainger, R.J., Barrass, J.D., Jacquier, A., Rain, J.-C., and Beggs, J.D. (2009). Physical and genetic
1105 interactions of yeast Cwc21p, an ortholog of human SRm300/SRRM2, suggest a role at the
1106 catalytic center of the spliceosome. RNA *15*, 2161–2173.

1107 Graser, S., Stierhof, Y.-D., Lavoie, S.B., Gassner, O.S., Lamla, S., Le Clech, M., and Nigg, E.A.
1108 (2007). Cep164, a novel centriole appendage protein required for primary cilium formation. J
1109 Cell Biol *179*, 321–330.

1110 Gunawardana, C.G., Mehrabian, M., Wang, X., Mueller, I., Lubambo, I.B., Jonkman, J.E.N.,
1111 Wang, H., and Schmitt-Ulms, G. (2015). The Human Tau Interactome: Binding to the
1112 Ribonucleoproteome, and Impaired Binding of the Proline-to-Leucine Mutant at Position 301
1113 (P301L) to Chaperones and the Proteasome. Mol. Cell Proteomics *14*, 3000–3014.

1114 Guthrie, C.R., Greenup, L., Leverenz, J.B., and Kraemer, B.C. (2011). MSUT2 is a determinant of
1115 susceptibility to tau neurotoxicity. Hum Mol Genet *20*, 1989–1999.

1116 Hales, C.M., Dammer, E.B., Diner, I., Yi, H., Seyfried, N.T., Gearing, M., Glass, J.D., Montine, T.J.,
1117 Levey, A.I., and Lah, J.J. (2014a). Aggregates of small nuclear ribonucleic acids (snRNAs) in
1118 Alzheimer's disease. Brain Pathol. *24*, 344–351.

1119 Hales, C.M., Seyfried, N.T., Dammer, E.B., Duong, D., Yi, H., Gearing, M., Troncoso, J.C., Mufson,
1120 E.J., Thambisetty, M., Levey, A.I., et al. (2014b). U1 small nuclear ribonucleoproteins (snRNPs)
1121 aggregate in Alzheimer's disease due to autosomal dominant genetic mutations and trisomy 21.
1122 Mol Neurodegener *9*, 15.

1123 Hanseeuw, B.J., Betensky, R.A., Jacobs, H.I.L., Schultz, A.P., Sepulcre, J., Becker, J.A., Cosio,
1124 D.M.O., Farrell, M., Quiroz, Y.T., Mormino, E.C., et al. (2019). Association of Amyloid and Tau
1125 With Cognition in Preclinical Alzheimer Disease: A Longitudinal Study. JAMA Neurol.

1126 Holmes, B.B., Furman, J.L., Mahan, T.E., Yamasaki, T.R., Mirbaha, H., Eades, W.C., Belaygorod,
1127 L., Cairns, N.J., Holtzman, D.M., and Diamond, M.I. (2014). Proteopathic tau seeding predicts
1128 tauopathy in vivo. Proc. Natl. Acad. Sci. U.S.A. *111*, E4376-4385.

1129   Hsieh, Y.-C., Guo, C., Yalamanchili, H.K., Abreha, M., Al-Ouran, R., Li, Y., Dammer, E.B., Lah, J.J.,
1130   Levey, A.I., Bennett, D.A., et al. (2019). Tau-Mediated Disruption of the Spliceosome Triggers
1131   Cryptic RNA Splicing and Neurodegeneration in Alzheimer's Disease. Cell Rep *29*, 301-316.e10.

1132   Huang, S., Deerinck, T.J., Ellisman, M.H., and Spector, D.L. (1994). In vivo analysis of the stability
1133   and transport of nuclear poly(A)+ RNA. J. Cell Biol. *126*, 877–899.

1134   Ilik, İ.A., Malszycki, M., Lübke, A.K., Schade, C., Meierhofer, D., and Aktaş, T. (2020). SON and
1135   SRRM2 are essential for nuclear speckle formation. ELife *9*, e60579.

1136   Jiang, L., Ash, P.E.A., Maziuk, B.F., Ballance, H.I., Boudeau, S., Abdullatif, A.A., Orlando, M.,
1137   Petrucelli, L., Ikezu, T., and Wolozin, B. (2019). TIA1 regulates the generation and response to
1138   toxic tau oligomers. Acta Neuropathol *137*, 259–277.

1139   Johnson, N.R., Condello, C., Guan, S., Oehler, A., Becker, J., Gavidia, M., Carlson, G.A., Giles, K.,
1140   and Prusiner, S.B. (2017). Evidence for sortilin modulating regional accumulation of human tau
1141   prions in transgenic mice. PNAS *114*, E11029–E11036.

1142   Kampers, T., Friedhoff, P., Biernat, J., Mandelkow, E.M., and Mandelkow, E. (1996). RNA
1143   stimulates aggregation of microtubule-associated protein tau into Alzheimer-like paired helical
1144   filaments. FEBS Lett. *399*, 344–349.

1145   Kaufman, S.K., Sanders, D.W., Thomas, T.L., Ruchinskas, A.J., Vaquer-Alicea, J., Sharma, A.M.,
1146   Miller, T.M., and Diamond, M.I. (2016). Tau Prion Strains Dictate Patterns of Cell Pathology,
1147   Progression Rate, and Regional Vulnerability In Vivo. Neuron *92*, 796–812.

1148   Khong, A., Matheny, T., Jain, S., Mitchell, S.F., Wheeler, J.R., and Parker, R. (2017). The Stress
1149   Granule Transcriptome Reveals Principles of mRNA Accumulation in Stress Granules. Molecular
1150   Cell *68*, 808-820.e5.

1151   Kinsella, R.J., Kähäri, A., Haider, S., Zamora, J., Proctor, G., Spudich, G., Almeida-King, J., Staines,
1152   D., Derwent, P., Kerhornou, A., et al. (2011). Ensembl BioMarts: a hub for data retrieval across
1153   taxonomic space. Database (Oxford) *2011*.

1154   Kiss, T. (2002). Small Nucleolar RNAs: An Abundant Group of Noncoding RNAs with Diverse
1155   Cellular Functions. Cell *109*, 145–148.

1156   Kota, K.P., Wagner, S.R., Huerta, E., Underwood, J.M., and Nickerson, J.A. (2008). Binding of ATP
1157   to UAP56 is necessary for mRNA export. Journal of Cell Science *121*, 1526–1537.

1158   Lagier-Tourenne, C., Polymenidou, M., Hutt, K.R., Vu, A.Q., Baughn, M., Huelga, S.C., Clutario,
1159   K.M., Ling, S.-C., Liang, T.Y., Mazur, C., et al. (2012). Divergent roles of ALS-linked proteins
1160   FUS/TLS and TDP-43 intersect in processing long pre-mRNAs. Nat. Neurosci. *15*, 1488–1497.

1161   Lee, G., Newman, S.T., Gard, D.L., Band, H., and Panchamoorthy, G. (1998). Tau interacts with
1162   src-family non-receptor tyrosine kinases. J. Cell. Sci. *111 (Pt 21)*, 3167–3177.

1163   Li, H.-D., Funk, C.C., and Price, N.D. (2020). iREAD: a tool for intron retention detection from
1164   RNA-seq data. BMC Genomics *21*, 128.

1165   Liu, C., and Götz, J. (2013). Profiling Murine Tau with 0N, 1N and 2N Isoform-Specific Antibodies
1166   in Brain and Peripheral Organs Reveals Distinct Subcellular Localization, with the 1N Isoform
1167   Being Enriched in the Nucleus. PLOS ONE *8*, e84849.

1168   Love, M.I., Huber, W., and Anders, S. (2014). Moderated estimation of fold change and
1169   dispersion for RNA-seq data with DESeq2. Genome Biology *15*, 550.

1170   Maj, M., Gartner, W., Ilhan, A., Neziri, D., Attems, J., and Wagner, L. (2010). Expression of TAU
1171   in insulin-secreting cells and its interaction with the calcium-binding protein secretagogin.
1172   Journal of Endocrinology *205*, 25–36.

1173   Maziuk, B.F., Apicco, D.J., Cruz, A.L., Jiang, L., Ash, P.E.A., da Rocha, E.L., Zhang, C., Yu, W.H.,
1174   Leszyk, J., Abisambra, J.F., et al. (2018). RNA binding proteins co-localize with small tau
1175   inclusions in tauopathy. Acta Neuropathol Commun *6*, 71.

1176   Meier, S., Bell, M., Lyons, D.N., Rodriguez-Rivera, J., Ingram, A., Fontaine, S.N., Mechas, E.,
1177   Chen, J., Wolozin, B., LeVine, H., et al. (2016). Pathological Tau Promotes Neuronal Damage by
1178   Impairing Ribosomal Function and Decreasing Protein Synthesis. J. Neurosci. *36*, 1001–1007.

1179   Montalbano, M., McAllen, S., Puangmalai, N., Sengupta, U., Bhatt, N., Johnson, O.D., Kharas,
1180   M.G., and Kayed, R. (2020). RNA-binding proteins Musashi and tau soluble aggregates initiate
1181   nuclear dysfunction. Nature Communications *11*, 4305.

1182   Motameny, S., Wolters, S., Nürnberg, P., and Schumacher, B. (2010). Next Generation
1183   Sequencing of miRNAs – Strategies, Resources and Methods. Genes (Basel) *1*, 70–84.

1184   Orr, M.E., Sullivan, A.C., and Frost, B. (2017). A Brief Overview of Tauopathy: Causes,
1185   Consequences, and Therapeutic Strategies. Trends Pharmacol Sci *38*, 637–648.

1186   Park, S.A., Ahn, S.I., and Gallo, J.-M. (2016). Tau mis-splicing in the pathogenesis of
1187   neurodegenerative disorders. BMB Rep *49*, 405–413.

1188   Polymenidou, M., Lagier-Tourenne, C., Hutt, K.R., Huelga, S.C., Moran, J., Liang, T.Y., Ling, S.-C.,
1189   Sun, E., Wancewicz, E., Mazur, C., et al. (2011). Long pre-mRNA depletion and RNA missplicing
1190   contribute to neuronal vulnerability from loss of TDP-43. Nature Neuroscience *14*, 459–468.

1191   Q, D., Wr, M., Q, C., F, L., and Jn, K. (2005). Ribosome dysfunction is an early event in
1192   Alzheimer's disease (J Neurosci).

1193   Rady, R.M., Zinkowski, R.P., and Binder, L.I. (1995). Presence of tau in isolated nuclei from
1194   human brain. Neurobiology of Aging *16*, 479–486.

1195 Raj, T., Li, Y.I., Wong, G., Humphrey, J., Wang, M., Ramdhani, S., Wang, Y.-C., Ng, B., Gupta, I.,
1196 Haroutunian, V., et al. (2018). Integrative transcriptome analyses of the aging brain implicate
1197 altered splicing in Alzheimer's disease susceptibility. Nat Genet *50*, 1584–1592.

1198 Ramaswami, M., Taylor, J.P., and Parker, R. (2013). Altered Ribostasis: RNA-Protein Granules in
1199 Degenerative Disorders. Cell *154*, 727–736.

1200 Rino, J., Carvalho, T., Braga, J., Desterro, J.M.P., Lührmann, R., and Carmo-Fonseca, M. (2007). A
1201 Stochastic View of Spliceosome Assembly and Recycling in the Nucleus. PLoS Computational
1202 Biology *3*.

1203 Sanders, D.W., Kaufman, S.K., DeVos, S.L., Sharma, A.M., Mirbaha, H., Li, A., Barker, S.J., Foley,
1204 A.C., Thorpe, J.R., Serpell, L.C., et al. (2014). Distinct tau prion strains propagate in cells and
1205 mice and define different tauopathies. Neuron *82*, 1271–1288.

1206 Santa-Maria, I., Varghese, M., Ksiezak-Reding, H., Dzhun, A., Wang, J., and Pasinetti, G.M.
1207 (2012). Paired helical filaments from Alzheimer disease brain induce intracellular accumulation
1208 of Tau protein in aggresomes. J. Biol. Chem. *287*, 20522–20533.

1209 Schmid-Burgk, J.L., Höning, K., Ebert, T.S., and Hornung, V. (2016). CRISPaint allows modular
1210 base-specific gene tagging using a ligase-4-dependent mechanism. Nature Communications *7*,
1211 12338.

1212 Schröder, H.C., Bernd, A., Zahn, R.K., and Müller, W.E. (1984). Binding of polyribonucleotides
1213 and polydeoxyribonucleotides to bovine brain microtubule protein: age-dependent modulation
1214 via phosphorylation of high-molecular-weight microtubule-associated proteins and tau
1215 proteins. Mech. Ageing Dev. *24*, 101–117.

1216 Sepulveda, G., Antkowiak, M., Brust-Mascher, I., Mahe, K., Ou, T., Castro, N.M., Christensen,
1217 L.N., Cheung, L., Jiang, X., Yoon, D., et al. (2018). Co-translational protein targeting facilitates
1218 centrosomal recruitment of PCNT during centrosome maturation in vertebrates. ELife *7*,
1219 e34959.

1220 Siano, G., Varisco, M., Caiazza, M.C., Quercioli, V., Mainardi, M., Ippolito, C., Cattaneo, A., and
1221 Di Primio, C. (2019). Tau Modulates VGluT1 Expression. Journal of Molecular Biology *431*, 873–
1222 884.

1223 Spector, D.L., and Lamond, A.I. (2011). Nuclear Speckles. Cold Spring Harb Perspect Biol *3*.

1224 Tanaka, H., Kondo, K., Chen, X., Homma, H., Tagawa, K., Kerever, A., Aoki, S., Saito, T., Saido, T.,
1225 Muramatsu, S.-I., et al. (2018). The intellectual disability gene PQBP1 rescues Alzheimer's
1226 disease pathology. Mol Psychiatry *23*, 2090–2110.

1227 Taylor, J.P., Brown, R.H., and Cleveland, D.W. (2016). Decoding ALS: from genes to mechanism.
1228 Nature *539*, 197–206.

1229 Ulrich, G., Salvadè, A., Boersema, P., Calì, T., Foglieni, C., Sola, M., Picotti, P., Papin, S., and
1230 Paganetti, P. (2018). Phosphorylation of nuclear Tau is modulated by distinct cellular pathways.
1231 Scientific Reports *8*, 1–14.

1232 Vanderweyde, T., Apicco, D.J., Youmans-Kidder, K., Ash, P.E.A., Cook, C., Lummertz da Rocha, E.,
1233 Jansen-West, K., Frame, A.A., Citro, A., Leszyk, J.D., et al. (2016). Interaction of tau with the
1234 RNA-Binding Protein TIA1 Regulates tau Pathophysiology and Toxicity. Cell Reports *15*, 1455–
1235 1466.

1236 Vaquero-Garcia, J., Barrera, A., Gazzara, M.R., González-Vallinas, J., Lahens, N.F., Hogenesch,
1237 J.B., Lynch, K.W., and Barash, Y. (2016). A new view of transcriptome complexity and regulation
1238 through the lens of local splicing variations. ELife *5*, e11752.

1239 Violet, M., Delattre, L., Tardivel, M., Sultan, A., Chauderlier, A., Caillierez, R., Talahari, S.,
1240 Nesslany, F., Lefebvre, B., Bonnefoy, E., et al. (2014). A major role for Tau in neuronal DNA and
1241 RNA protection in vivo under physiological and hyperthermic conditions. Front Cell Neurosci *8*,
1242 84.

1243 Violet, M., Chauderlier, A., Delattre, L., Tardivel, M., Chouala, M.S., Sultan, A., Marciniak, E.,
1244 Humez, S., Binder, L., Kayed, R., et al. (2015). Prefibrillar Tau oligomers alter the nucleic acid
1245 protective function of Tau in hippocampal neurons in vivo. Neurobiol. Dis. *82*, 540–551.

1246 Wagner, S., Chiosea, S., Ivshina, M., and Nickerson, J.A. (2004). In vitro FRAP reveals the ATP-
1247 dependent nuclear mobilization of the exon junction complex protein SRm160. J Cell Biol *164*,
1248 843–850.

1249 Wang, X., Wang, D., Zhao, J., Qu, M., Zhou, X., He, H., and He, R. (2006). The proline-rich
1250 domain and the microtubule binding domain of protein tau acting as RNA binding domains.
1251 Protein Pept. Lett. *13*, 679–685.

1252 Wegmann, S., Medalsy, I.D., Mandelkow, E., and Müller, D.J. (2013). The fuzzy coat of
1253 pathological human Tau fibrils is a two-layered polyelectrolyte brush. Proc. Natl. Acad. Sci.
1254 U.S.A. *110*, E313-321.

1255 Wheeler, J.M., McMillan, P., Strovas, T.J., Liachko, N.F., Amlie-Wolf, A., Kow, R.L., Klein, R.L.,
1256 Szot, P., Robinson, L., Guthrie, C., et al. (2019). Activity of the poly(A) binding protein MSUT2
1257 determines susceptibility to pathological tau in the mammalian brain. Science Translational
1258 Medicine *11*.

1259 Wingett, S.W., and Andrews, S. (2018). FastQ Screen: A tool for multi-genome mapping and
1260 quality control. F1000Res *7*.

1261 Wischik, C.M., Novak, M., Thøgersen, H.C., Edwards, P.C., Runswick, M.J., Jakes, R., Walker, J.E.,
1262 Milstein, C., Roth, M., and Klug, A. (1988). Isolation of a fragment of tau derived from the core
1263 of the paired helical filament of Alzheimer disease. Proc Natl Acad Sci U S A *85*, 4506–4510.

1264 Woerman, A.L., Aoyagi, A., Patel, S., Kazmi, S.A., Lobach, I., Grinberg, L.T., McKee, A.C., Seeley,
1265 W.W., Olson, S.H., and Prusiner, S.B. (2016). Tau prions from Alzheimer's disease and chronic
1266 traumatic encephalopathy patients propagate in cultured cells. PNAS.

1267 Xu, H., Yao, J., Wu, D.C., and Lambowitz, A.M. (2019). Improved TGIRT-seq methods for
1268 comprehensive transcriptome profiling with decreased adapter dimer formation and bias
1269 correction. Scientific Reports *9*, 1–17.

1270 Yoshiyama, Y., Higuchi, M., Zhang, B., Huang, S.-M., Iwata, N., Saido, T.C., Maeda, J., Suhara, T.,
1271 Trojanowski, J.Q., and Lee, V.M.-Y. (2007). Synapse loss and microglial activation precede
1272 tangles in a P301S tauopathy mouse model. Neuron *53*, 337–351.

1273 Zhang, Q., Kota, K.P., Alam, S.G., Nickerson, J.A., Dickinson, R.B., and Lele, T.P. (2016).
1274 Coordinated dynamics of RNA splicing speckles in the nucleus. J Cell Physiol *231*, 1269–1275.

1275 Zhang, W., Tarutani, A., Newell, K.L., Murzin, A.G., Matsubara, T., Falcon, B., Vidal, R., Garringer,
1276 H.J., Shi, Y., Ikeuchi, T., et al. (2020). Novel tau filament fold in corticobasal degeneration.
1277 Nature 1–7.

1278 Zhang, X., Lin, Y., Eschmann, N.A., Zhou, H., Rauch, J.N., Hernandez, I., Guzman, E., Kosik, K.S.,
1279 and Han, S. (2017). RNA stores tau reversibly in complex coacervates. PLoS Biol *15*.

1280 Zhang, X., Yan, C., Zhan, X., Li, L., Lei, J., and Shi, Y. (2018). Structure of the human activated
1281 spliceosome in three conformational states. Cell Research *28*, 307–322.

1282 Zimowska, G., Shi, J., Munguba, G., Jackson, M.R., Alpatov, R., Simmons, M.N., Shi, Y., and
1283 Sugrue, S.P. (2003). Pinin/DRS/memA Interacts with SRp75, SRm300 and SRrp130 in Corneal
1284 Epithelial Cells. Invest. Ophthalmol. Vis. Sci. *44*, 4715–4723.

1285

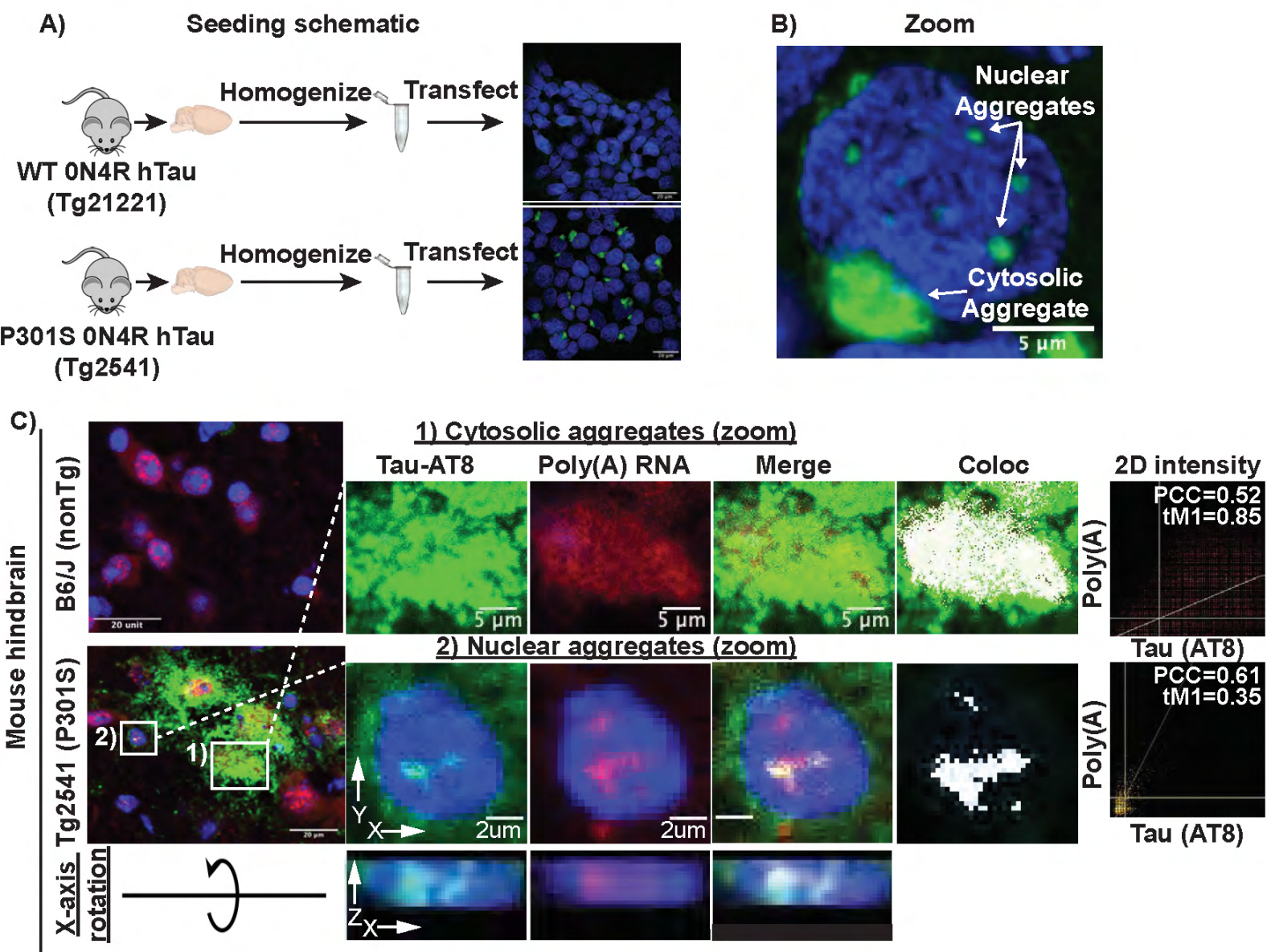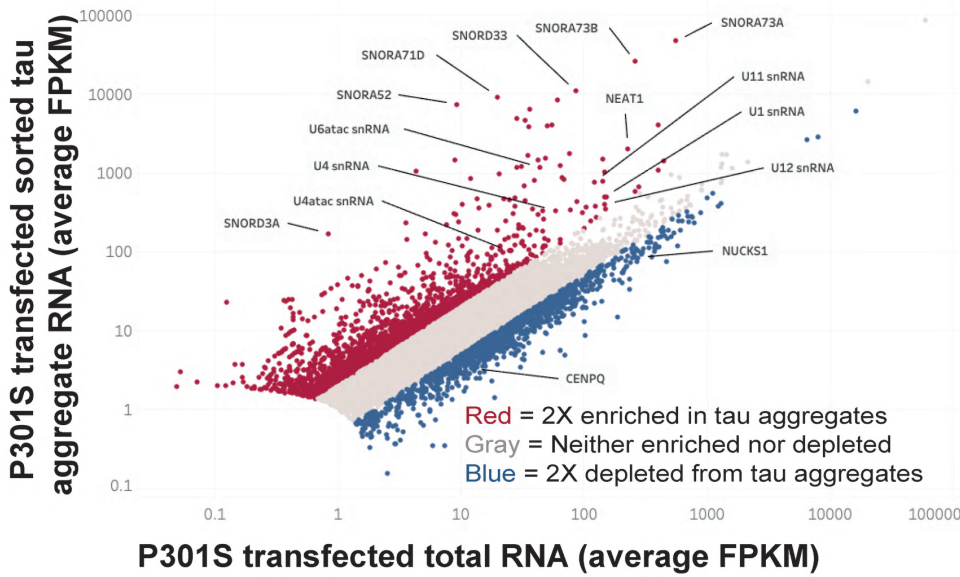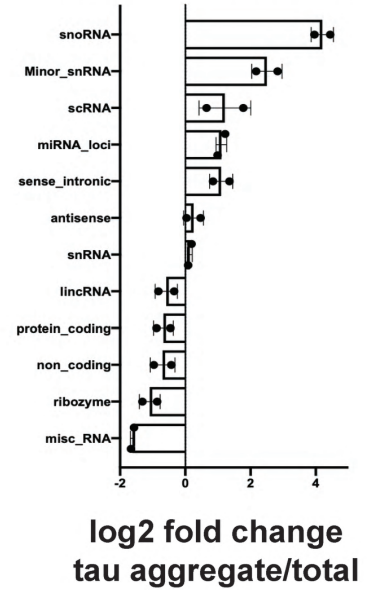**Figure 1: Tau biosensor cell schematic and tau aggregates in mice contain poly(A) RNA.**

Figure 2: The RNA composition of tau aggregates in cellular and mouse tauopathy model systems.
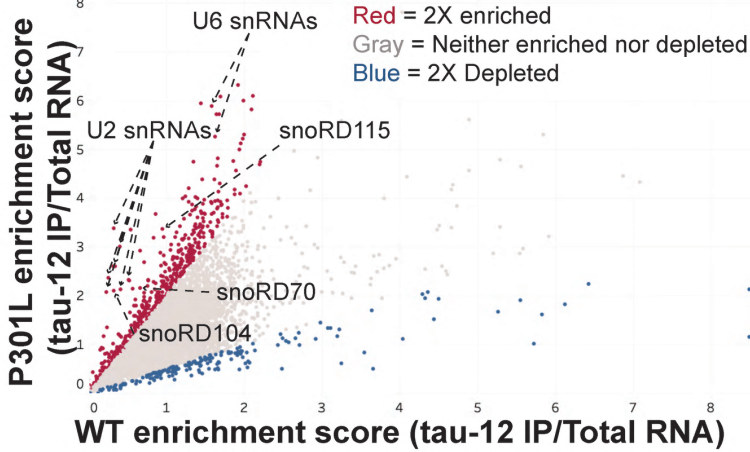

A) RNAs enriched in tau aggregates from HEK293 biosensor cells

B) Gene type enrichment in HEK293 tau aggregates

C) RNAs associated with tau aggregates in P301L mice and WT mice
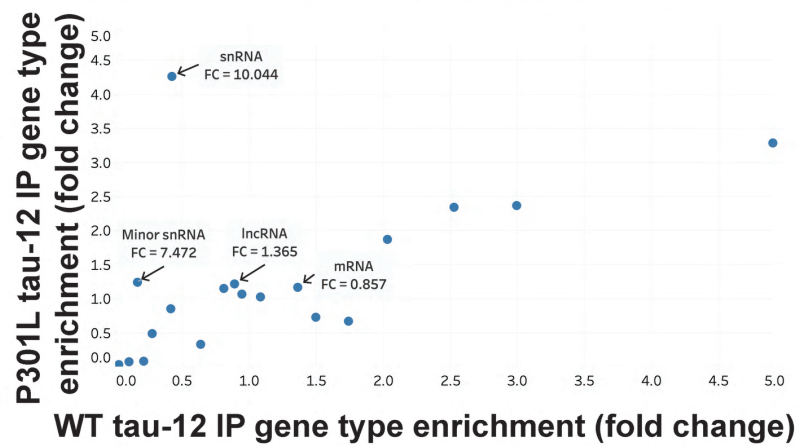
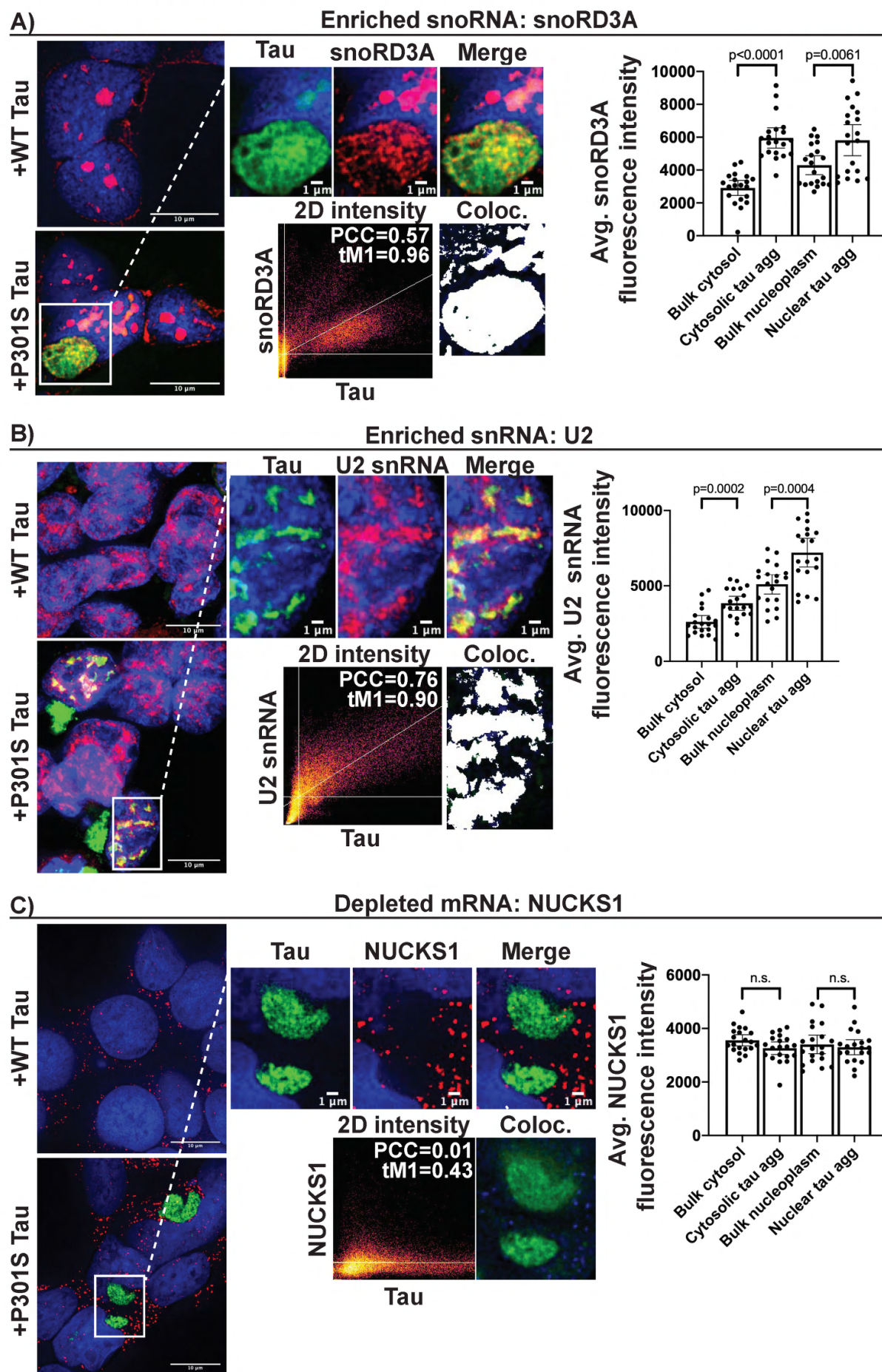**D)** P301L vs WT tau-12 IP gene type enrichment

Figure 3: FISH for RNAs in HEK293 tau biosensor cells

Figure 4: Tau aggregates colocalize with splicing speckles and mislocalize SRRM2 in tauopathy model systems.

A)

Tau RD-CFP/YFP | SRRM2 | Merge

+WT Tau

+P301S Tau

HEK293 tau biosensor cells

B) 1) Nuclear aggregates (colocalized)
PCC=0.93
tM1=0.87

2) Cytosolic aggregates (colocalized)
PCC=0.89
tM1=0.94

3) Cytosolic aggregates (not colocalized)
No positive correlations found

C) Tau aggregates decrease % of nuclear SRRM2 in HEK293 cells
p < 0.0001

D) H4 neuronal cells 0N4R*P301S-YFP
Uninfected
+P301S Tau

1) Zoom of SRRM2 heterogeneity in tau aggregates
pTau (Thr205) | SRRM2 | Coloc

2) Zoom of SRRM2 nuclear depletion
pTau (Thr205) | SRRM2 | Merge

E) 2D Intensity plot

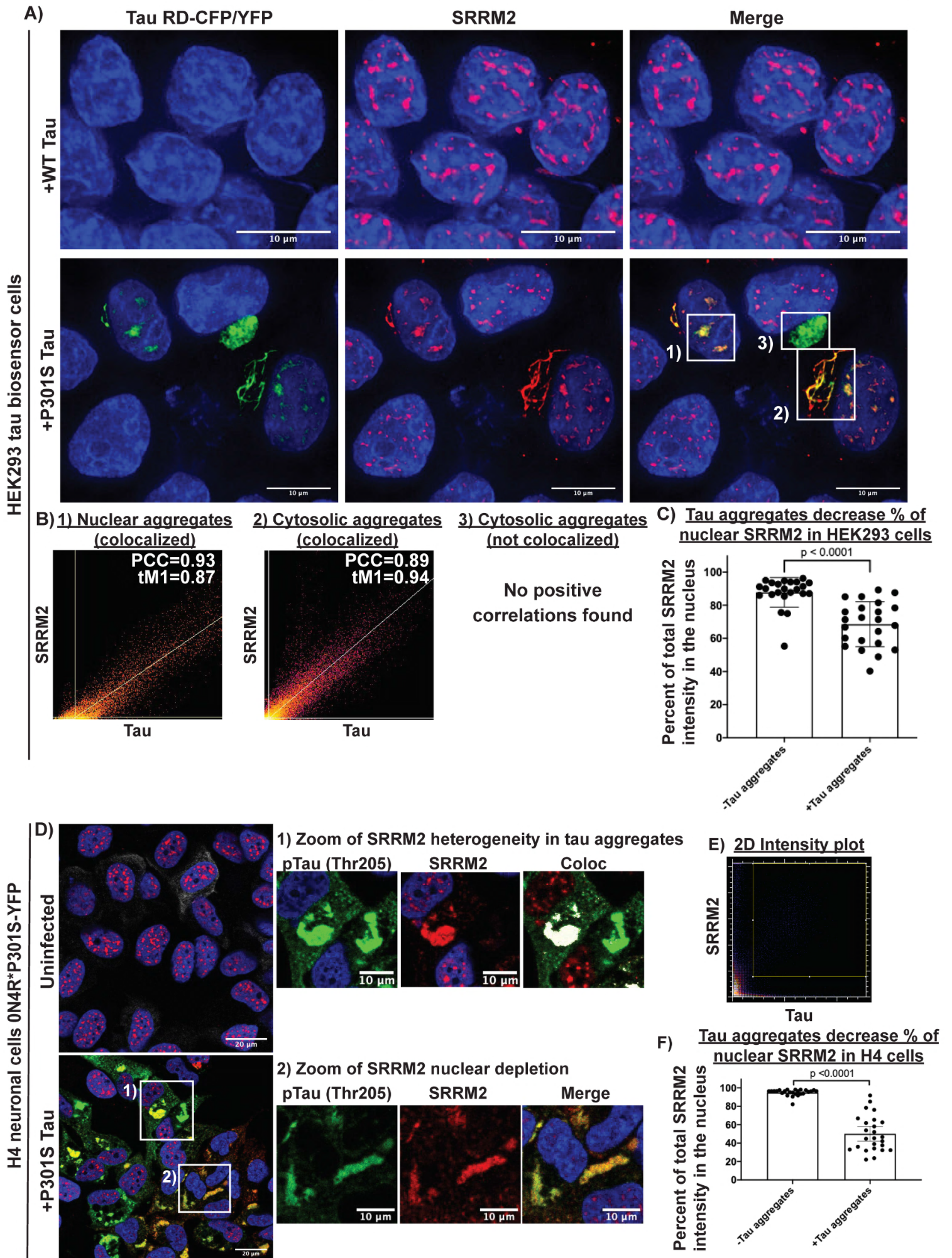F) Tau aggregates decrease % of nuclear SRRM2 in H4 cells
p <0.0001

Figure 5: Other proteins that localize to tau aggregates and the c-terminal region of SRRM2 is responsible for localization to tau aggregates.
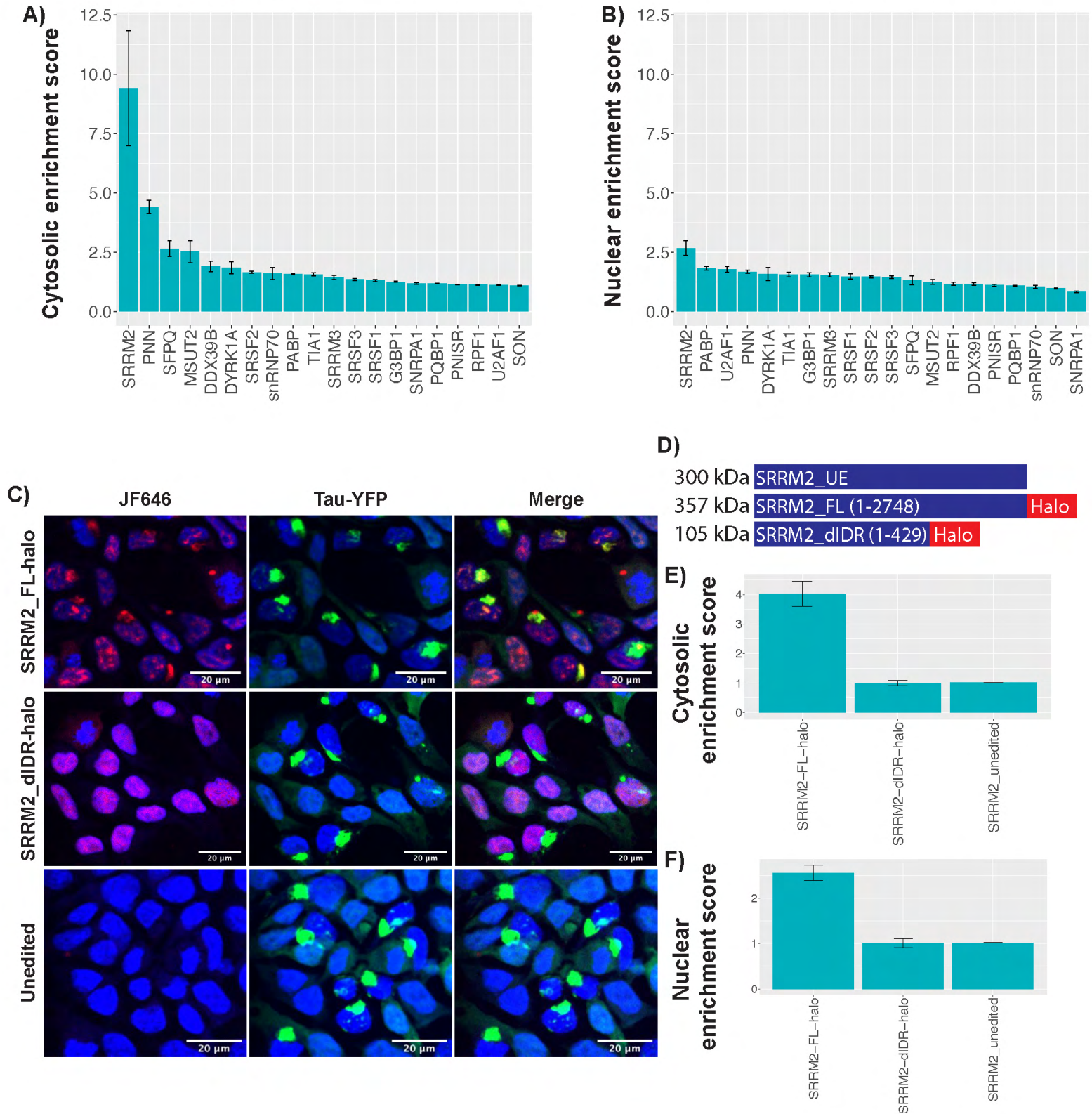
Figure 6: Tau aggregation alters dynamics and organization of splicing speckles and RNA splicing.
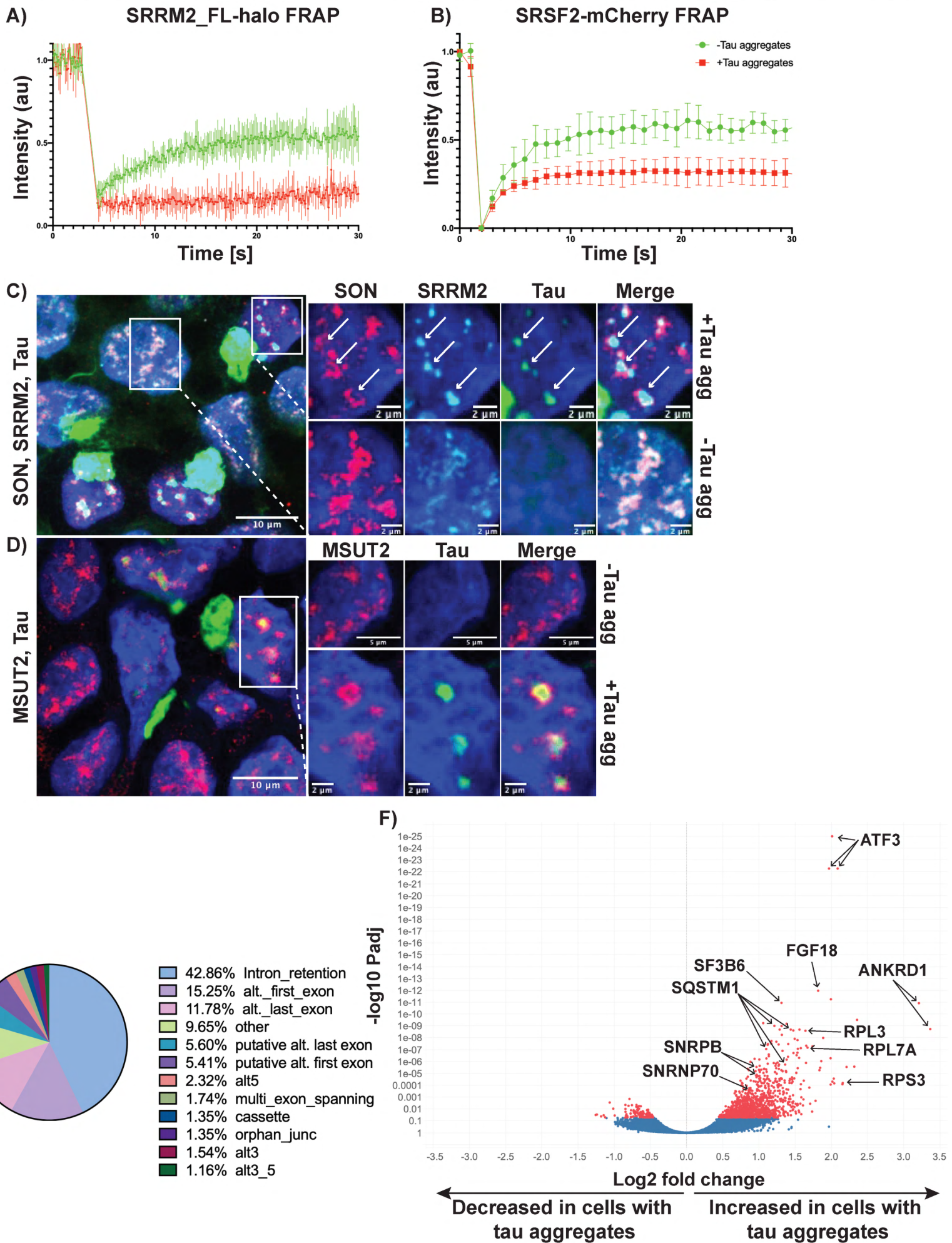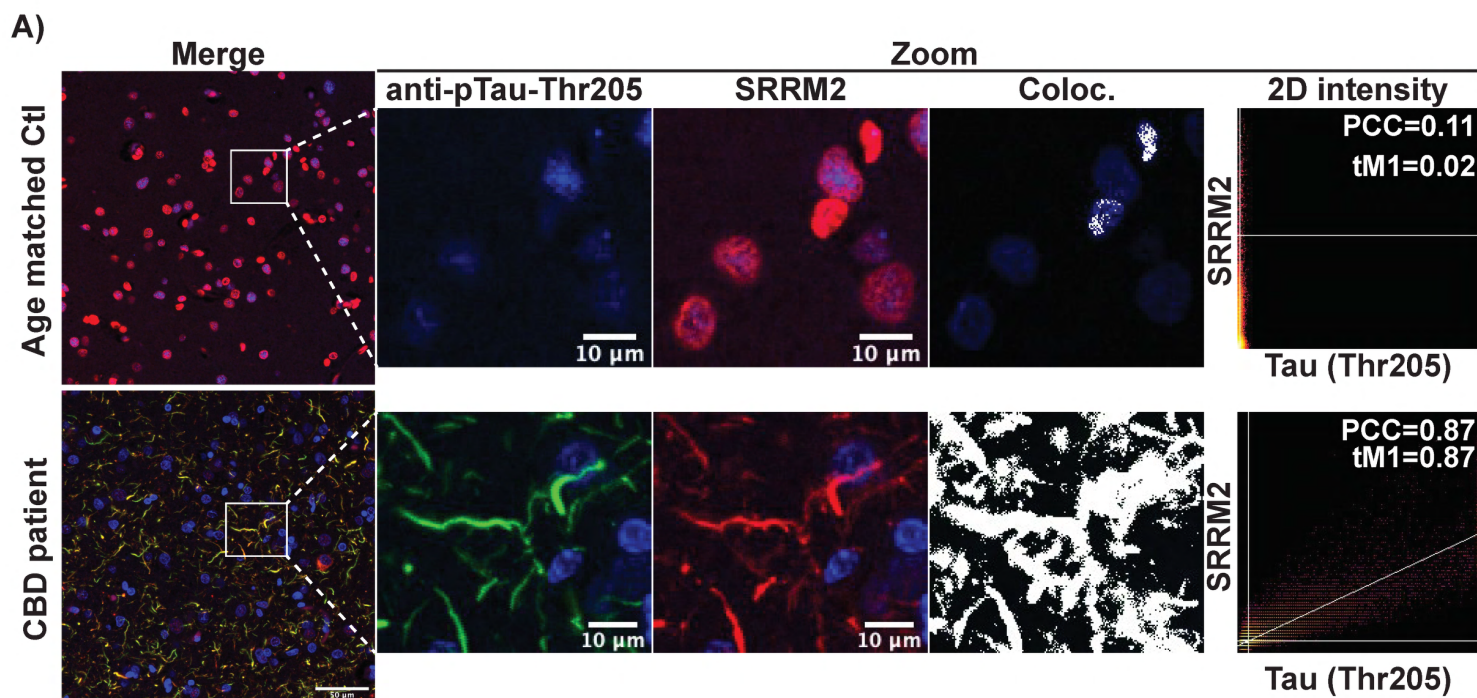
Figure 7: SRRM2 is relocalized to cytosolic tau aggregates in human tauopathies

A) Merge / Zoom / anti-pTau-Thr205 / SRRM2 / Coloc. / 2D intensity

Age matched Ctl — PCC=0.11, tM1=0.02, SRRM2, Tau (Thr205)

CBD patient — PCC=0.87, tM1=0.87, SRRM2, Tau (Thr205)

B) SRRM2 nuclear depletion
p<0.0001
Average Nuclear SRRM2 Intensity
Control / CBD

C) Human brain SRRM2 IHC
Control1 / AD1 / FTLD1
Control2 / AD2 / FTLD2
20uM